Macrophage fumarate hydratase restrains mtRNA-mediated interferon production

Alexander Hooftman[1,13], **Christian G. Peace**[1,13], **Dylan G. Ryan**[1,2,3,13], **Emily A. Day**[1], **Ming Yang**[2,4], **Anne F. McGettrick**[1], **Maureen Yin**[1], **Erica N. Montano**[5,6], **Lihong Huo**[5,6], **Juliana E. Toller-Kawahisa**[1,7], **Vincent Zecchini**[2], **Tristram A. J. Ryan**[1], **Alfonso Bolado-Carrancio**[8], **Alva M. Casey**[3], **Hiran A. Prag**[3], **Ana S. H. Costa**[2,9], **Gabriela De Los Santos**[5], **Mariko Ishimori**[5,10], **Daniel J. Wallace**[5,10], **Swamy Venuturupalli**[5], **Efterpi Nikitopoulou**[2], **Norma Frizzell**[11], **Cecilia Johansson**[12], **Alexander Von Kriegsheim**[8], **Michael P. Murphy**[3], **Caroline Jefferies**[5,6], **Christian Frezza**[2,4], **Luke A. J. O'Neill**[1]

[1]School of Biochemistry and Immunology, Trinity Biomedical Sciences Institute, Trinity College Dublin, Dublin, Ireland.

[2]MRC Cancer Unit, University of Cambridge, Cambridge, UK.

[3]MRC Mitochondrial Biology Unit, University of Cambridge, Cambridge, UK.

[4]CECAD Research Centre, Faculty of Medicine, University of Cologne, Cologne, Germany.

[5]Division of Rheumatology, Department of Medicine, Cedars–Sinai Medical Center, Los Angeles, CA, USA.

[6]Department of Biomedical Sciences, Cedars–Sinai Medical Center, Los Angeles, CA, USA.

[7]Department of Pharmacology, Ribeirao Preto Medical School, University of Sao Paulo, Sao Paulo, Brazil.

[8]Edinburgh Cancer Research UK Centre, University of Edinburgh, Edinburgh, UK.

[9]Matterworks, Somerville, MA, USA.

[10]David Geffen School of Medicine, University of California Los Angeles, Los Angeles, CA, USA.

[11]School of Medicine, University of South Carolina, Columbia, SC, USA.

[12]National Heart and Lung Institute, Imperial College London, London, UK.

[13]These authors contributed equally: Alexander Hooftman, Christian G. Peace, Dylan G. Ryan.

Abstract

Metabolic rewiring underlies the effector functions of macrophages[1–3], but the mechanisms involved remain incompletely defined. Here, using unbiased metabolomics and stable isotope-assisted tracing, we show that an inflammatory aspartate–argininosuccinate shunt is induced following lipopolysaccharide stimulation. The shunt, supported by increased argininosuccinate synthase (ASS1) expression, also leads to increased cytosolic fumarate levels and fumarate-mediated protein succination. Pharmacological inhibition and genetic ablation of the tricarboxylic acid cycle enzyme fumarate hydratase (FH) further increases intracellular fumarate levels. Mitochondrial respiration is also suppressed and mitochondrial membrane potential increased. RNA sequencing and proteomics analyses demonstrate that there are strong inflammatory effects resulting from FH inhibition. Notably, acute FH inhibition suppresses interleukin-10 expression, which leads to increased tumour necrosis factor secretion, an effect recapitulated by fumarate esters. Moreover, FH inhibition, but not fumarate esters, increases interferon-β production through mechanisms that are driven by mitochondrial RNA (mtRNA) release and activation of the RNA sensors TLR7, RIG-I and MDA5. This effect is recapitulated endogenously when FH is suppressed following prolonged lipopolysaccharide stimulation. Furthermore, cells from patients with systemic lupus erythematosus also exhibit FH suppression, which indicates a potential pathogenic role for this process in human disease. We therefore identify a protective role for FH in maintaining appropriate macrophage cytokine and interferon responses.

Stimulation of macrophages with the TLR4 ligand lipopolysaccharide (LPS) leads to reprogramming of central metabolic pathways involved in bioenergetics, which can facilitate cytokine production. Changes in macrophage metabolism have emerged as a major regulator of inflammation[1–7]. Although metabolic reprogramming is crucial for macrophage activation the players involved and how they regulate cytokine production remain incompletely characterized.

Accumulation of fumarate in macrophages

To evaluate metabolic alterations that occur during LPS stimulation, we used an unbiased metabolomics approach based on liquid chromatography–mass spectrometry to characterize the metabolome of inflammatory bone-marrow-derived macrophages (BMDMs). The TCA cycle metabolite fumarate stood out as one of the most significantly upregulated metabolites following exposure to acute LPS stimulation, joining previously identified metabolites such as itaconate[2] (Fig. 1a). We also observed a significant increase in fumarate-mediated protein succination[8–10], which resulted in the formation of the fumarate-cysteine adduct (S)-2-succinocysteine (2SC) (Extended Data Fig. 1a–c).

As acute LPS stimulation failed to impair respiration (Fig. 1b,c), TCA cycle disruption is unlikely to be sufficient for fumarate accumulation. Increased flux through the aspartate–argininosuccinate shunt has been reported to support nitric oxide production[5]. As fumarate is a by-product of argininosuccinate cleavage by argininosuccinate lyase (ASL) in the cytosol, we proposed that argininosuccinate may be a source of fumarate. In support of this hypothesis, we observed decreased aspartate, the precursor to argininosuccinate, and increased argininosuccinate, fumarate and malate levels (Fig. 1d), a result consistent with increased flux through the shunt. This rewiring also occurred during prolonged LPS stimulation (Extended Data Fig. 1d).

Argininosuccinate synthase (*Ass1*) and FH (encoded by *Fh1* in mice and *FH* in humans) expression increased and decreased, respectively in LPS-stimulated BMDMs, as determined by quantitative PCR with reverse transcription (RT–qPCR) (Fig. 1e). Analyses of available quantitative proteomics data[2,11] showed that ASS1 was upregulated, whereas levels of glutamic-oxaloacetic transaminase 2 (GOT2), ASL and FH were not significantly altered (Fig. 1f). FH levels were suppressed only at later time points of LPS treatment (Fig. 1g), which indicates that ASS1 induction is vital to the acute accumulation of fumarate.

Inhibition of the aspartate–argininosuccinate shunt with the GOT2 inhibitor aminooxyacetic acid (AOAA)[5] reduced aspartate, asparagine, argininosuccinate and fumarate levels following LPS stimulation (Fig. 1h and Extended Data Fig. 1e). Knockdown of *Asl* also prevented fumarate accumulation (Extended Data Fig. 1f,g), which indicated the dependency of fumarate production on the aspartate–argininosuccinate shunt, which would increase cytosolic fumarate levels (Fig. 1i). Stable isotope-assisted tracing showed that glutamine-dependent anaplerosis is in part responsible for fumarate accumulation and drives the aspartate–argininosuccinate shunt. U-^{13}C-glutamine tracing demonstrated glutaminolysis as a carbon source for the TCA cycle, aspartate–argininosuccinate shunt metabolites, including fumarate, and glutathione (Extended Data Fig. 2). ^{15}N$_2$-glutamine tracing also demonstrated that glutamine nitrogen is a source for glutathione synthesis and aspartate–argininosuccinate shunt metabolites (Extended Data Fig. 3). Notably, AOAA prevented the contribution of glutamine nitrogen to aspartate, asparagine, arginine and citrulline, thereby confirming its inhibition of GOT2. Metabolomics analysis of cytosolic fractions of resting and LPS-stimulated macrophages showed that metabolites such as itaconate and succinate accumulated in the cytosol following LPS stimulation (Extended Data Fig. 4a). Increased levels of argininosuccinate, fumarate and 2SC were also present in the cytosol (Extended Data Fig. 4b).

We proposed that *Irg1*$^{−/−}$ BMDMs (which are unable to synthesize itaconate) would relieve the inhibition of succinate dehydrogenase[4,12] and exhibit greater accumulation of aspartate–argininosuccinate shunt metabolites. Metabolomics analysis of *Irg1*$^{−/−}$ BMDMs revealed the expected decrease in itaconate and succinate levels, and increased aspartate–argininosuccinate shunt metabolites, including fumarate and nitric oxide (Extended Data Fig. 4c,d). This result provides further evidence linking mitochondrial TCA cycle activity to an aspartate–argininosuccinate shunt (Extended Data Fig. 4e).

FH inhibition causes metabolic rewiring

FH catalyses the hydration of fumarate to malate in mitochondria and the cytosol[13]. Inhibition of this process increases cytosolic fumarate accumulation, perturbs urea cycle metabolism and leads to renal cyst development[14]. FH levels remained stable during early LPS stimulation (Fig. 1g). Therefore, we used a well-established pharmacological inhibitor of FH (FHIN1)[15] and a recently developed tamoxifen-inducible model of *cre-ERT2*-expressing *Fh1*−/− mice to analyse the role of FH activity and fumarate accumulation in macrophages. However, because FH inhibition may lead to effects independent of fumarate accumulation through mitochondrial and redox stress[16], we also used low concentrations of cell-permeable dimethyl fumarate (DMF) to deliver a cysteine-reactive fumarate ester, which does not inhibit respiration[17–19]. This approach uncouples the role of impaired mitochondrial bioenergetics following TCA cycle disruption and fumarate-mediated electrophilic modification of cysteine residues.

Previous reports have shown that immunometabolites and their derivatives affect macrophage function through the regulation of metabolic pathways[4,9,20]. We therefore aimed to assess how FH inhibition and DMF may regulate macrophage metabolism. First, comparing the effects of FHIN1 and DMF on mitochondrial bioenergetics, we found that FHIN1 reduced ratios of ATP/ADP, ATP/AMP and P-creatine/creatine. By contrast, DMF had little effect, which demonstrates that FH sustains mitochondrial bioenergetics (Fig. 2a and Extended Data Fig. 5a). This result was confirmed through respirometry experiments, which showed that FHIN1 impaired basal respiration, ATP production and maximal respiration, as measured by oxygen consumption rates, whereas DMF had no effect (Fig. 2b). FHIN1 led to a distinct metabolic signature characterized by alterations in TCA cycle metabolites, including citrate, aconitate, itaconate and succinate. This result indicates that the TCA cycle is rewired and enhances fumarate and 2SC accumulation, and provides support for using this approach to study the roles of FH in macrophages (Fig. 2c,e and Extended Data Fig. 5b). Principal component analysis showed significant divergence of FHIN1 treatment to the other conditions (Fig. 2d).

Tamoxifen-inducible knockout of *Fh1* in macrophages (Extended Data Fig. 5c,d) induced similar bioenergetic changes as those induced by FHIN1, such as reduced ATP/AMP and P-creatine/creatine ratios, although the ATP/ADP ratio was unchanged (Extended Data Fig. 5e). TCA cycle rewiring was also observed in *Fh1*−/− macrophages, although to a lesser extent than with FHIN1 (Extended Data Fig. 5f). Compensatory remodelling during initial genetic inactivation of FH may buffer some of the acute changes observed with FHIN1 (ref. [21]). However, fumarate and 2SC levels were increased in *Fh1*−/− macrophages (Fig. 2f and Extended Data Fig. 5g), which provides support for our parallel use of FHIN1 and *Fh1*−/− macrophages.

Confirming previous reports[9], DMF, and to a lesser extent FHIN1, suppressed glycolysis (Extended Data Fig. 5h). GAPDH is reportedly inhibited by fumarate-mediated succination[9,22]. Consistently, FHIN1 increased the ratio of glyceraldehyde 3-phosphate to 2/3- phosphoglycerate (G3P/2/3-PG) (Extended Data Fig. 5i), which suggests that

endogenous fumarate accumulation may impair GAPDH activity. This result provides further evidence that FH impairment leads to the modulation of cytosolic processes.

As FHIN1 impaired respiration, we examined additional mitochondrial parameters. We first observed increased reactive oxygen species production in cells treated with FHIN1 but not DMF (Fig. 2g). FHIN1 treatment also increased the staining intensity of the mitochondrial membrane potential (MMP)-dependent dye Mitotracker Red (Extended Data Fig. 5j,k). Tetramethylrhodamine methyl ester (TMRM) staining confirmed this result, as FHIN1 significantly increased staining, whereas DMF had no effect (Fig. 2h). Similarly, $Fh1^{-/-}$ macrophages had increased MMP values, as previously reported in kidney epithelial cells[23] (Fig. 2h). We also observed a decreased aconitate/citrate ratio in FHIN1-treated macrophages, which was indicative of impairment in the fumarate-sensitive and redox-sensitive TCA cycle enzyme aconitase[24] (Fig. 2i). Although the GSSG/GSH ratio was unchanged, FHIN1 led to a depletion of total glutathione (Fig. 2j), which is consistent with fumarate-mediated glutathione depletion[25,26]. These data suggest that FH inhibition induces substantial redox stress responses.

FH maintains appropriate cytokine responses

To determine whether FH regulates macrophage activation and effector responses, we performed RNA sequencing (RNA-seq) and proteomics to assess changes in the transcriptome and proteome of FHIN1-treated BMDMs. Gene set enrichment analysis (GSEA) identified an expected suppression in genes associated with metabolism. However, FHIN1 also decreased the expression of pathways that affect inflammation, including interleukin-1 (IL-1) and IL-10 signalling (Fig. 3a). Increased expression of components of the haem-regulated inhibitor stress response, amino acid metabolism and tRNA aminoacylation was also observed (Fig. 3a), consistent with previous reports[16]. Overrepresentation analysis of RNA-seq data revealed that tumour necrosis factor (TNF) signalling was the most highly upregulated pathway in our analysis (Fig. 3b).

Comparing FHIN1 with DMF on cytokine readouts allowed us to determine the role of protein succination following FH inhibition. FHIN1 and DMF decreased IL-10 release and expression, whereas TNF release and expression were increased (Fig. 3c and Extended Data Fig. 6a). This result validated our transcriptomics analysis. Both compounds also reduced IL-1β expression and IL-6 release (Extended Data Fig. 6b), consistent with previous reports[10,27], thereby demonstrating the wide-spread regulation of cytokine expression.

The less electrophilic fumarate ester monomethyl fumarate (MMF) exhibited the same effects on *Il10* and *Tnf* expression (Fig. 3d), which provides support for a role for fumarate in their regulation. Shared transcriptomic changes induced by FHIN1 and DMF demonstrated strong downregulation of the ERK1 and ERK2 cascade and PI3K signalling (Fig. 3e). A similar transcriptional fingerprint has been observed in FH-deficient leiomyomas[28]. We also observed increased amino acid metabolism and transport and autophagy transcripts (Extended Data Fig. 6c). Following LPS stimulation, IL-10 is regulated by ERK1 and ERK2 and PI3K-induced AP-1 activation[29], which suggests that downregulation of this signalling axis by FHIN1 and DMF may repress IL-10. However,

we did not observe changes in the upstream kinases AKT, JNK, ERK and p38, which converge on AP-1 activation (Extended Data Fig. 6d). Although we did observe reduced *Jun* expression in our transcriptomics dataset (Extended Data Fig. 6e), this could indicate reduced autoregulation by AP-1 (ref. [30]). In this dataset, *Fos* was not reduced (Extended Data Fig. 6f).

Notably, the thiol precursor *N*-acetyl cysteine (NAC) abrogated the suppression of *Il10* by FHIN1 and DMF (Fig. 3f). The free thiols of NAC and its products would react with and sequester fumarate, thereby reducing the modification of protein thiols and suggesting that suppression of IL-10 results from a redox-dependent succination event. The electrophile sulforaphane has been shown to reduce AP-1 activation through the modification of Cys154 on c-Fos[31]. We therefore investigated whether FHIN1 or DMF may affect c-Fos activation, despite upstream regulators remaining unaffected. c-Fos transcription factor assays showed that FHIN1 and DMF strongly impaired c-Fos activation (Fig. 3g), which provides evidence of direct regulation of c-Fos, potentially through S-alkylation.

IL-10 signalling has been shown to repress TNF expression[32]. We confirmed this effect using an IL-10 receptor (CD210) blocking antibody that targets IL-10-mediated STAT3 phosphorylation. This blockade leads to augmented LPS-induced TNF release (Fig. 3h and Extended Data Fig. 6g). We then examined whether recombinant IL-10 supplementation could rescue the increase in TNF release. IL-10 with FHIN1 failed to impair STAT3 phosphorylation or augment TNF production (Fig. 3i,j), which indicates that the induction of TNF driven by FHIN1 or DMF depends on the suppression of IL-10.

We sought to confirm the role of FH in regulating this axis. Inducible deletion of *Fh1* in macrophages from heterozygous *Fh1*$^{+/-}$ or homozygous *Fh1*$^{-/-}$ mice (Extended Data Figs. 5c,d and 6h) resulted in decreased IL-10 expression and release (Fig. 3k) and increased TNF release (Fig. 3l). Furthermore, FHIN1 also suppressed *IL10* expression and increased *TNF* expression in LPS-stimulated human peripheral blood mononuclear cells (PBMCs) (Fig. 3m) and macrophages (Fig. 3n). This result indicates that the FH-regulated IL-10–TNF axis is also active in human cells. Establishing the role of LPS-driven fumarate accumulation in the release of these cytokines, AOAA, which reduces fumarate accumulation (Fig. 1h), modestly increased and reduced IL-10 and TNF release, respectively (Extended Data Fig. 6i). This result indicates that an increase in ASS1, which results in fumarate accumulation, mildly regulates IL-10 and TNF production. These effects were accentuated by pharmacological or genetic inhibition of FH, which led to increased fumarate accumulation (Extended Data Fig. 6j). Therefore, sustained expression and activity of FH may be viewed as protective against excessive fumarate accumulation and dysregulated production of IL-10 and TNF.

FH inhibition also resulted in the activation of a NRF2 and ATF4 stress response in macrophages (Extended Data Fig. 7a), which is in line with previous observations in epithelial cells[16]. Proteomics analysis revealed that the inflammation-associated hormone GDF15 (refs. [33–35]) was one of the most significantly increased proteins following FHIN1 and DMF treatment, whereas FHIN1 also increased the recently identified mitochondrial glutathione importer SLC25A39 (ref.[36]). This result reinforces the fact that mitochondrial

redox is perturbed (Extended Data Fig. 7b,c). In support of our proteomics data, FH inhibition drove GDF15 release from macrophages (Extended Data Fig. 7d). Both ATF4 and NRF2 have been reported to regulate GDF15 in different contexts[34,37], and silencing of each revealed that FHIN1-driven GDF15 release partly depended on NRF2 but not ATF4 (Extended Data Fig. 7e,f). This work defines two previously unappreciated signalling axes linked to FH inhibition, uncovering its role in the regulation of IL-10, TNF and GDF15. Recent developments that have identified GDF15 as a mediator of immune tolerance, and the anti-inflammatory properties of colchicine and nonsteroidal anti-inflammatory drugs[37,38], suggest that protective effects of DMF in models of inflammation could be mediated at least in part through GDF15. Moreover, increased TNF levels potentially explain adverse events reported with fumarate esters[39]. Mechanistically, suppression of IL-10 may also explain why fumarate esters promote enhanced TNF production during trained immunity, in addition to reported epigenetic changes[40].

FH restrains mtRNA-driven IFNβ release

RNA-seq analysis of type I interferon (IFN) response genes revealed divergent effects on IFN expression and signalling following FH inhibition, including an upregulation in *Ifnb1* (which encodes IFNβ) expression and several interferon-stimulated genes, such as *Irf1*, *Ifih1, Rsad2* and *Ifit2* (Fig. 4a). However, other interferon-stimulated genes, such as *Lcn2*, were suppressed by FHIN1 and DMF treatment (Fig. 4a and Extended Data Fig. 8a). Examination of specific type I IFN signalling components downstream of the IFNα/β receptor (IFNAR) revealed that both FHIN1 and DMF treatment limited IFNβ-induced STAT1 and JAK1 phosphorylation (Extended Data Fig. 8b), which indicated that there was modest suppression of JAK–STAT signalling. Activation of NRF2 by fumarate and derivatives (Extended Data Fig. 7) may be responsible[41]. Indeed, *Ifnb1* expression was increased after FHIN1 and DMF treatment following *Nrf2* silencing (Extended Data Fig. 8c,d), which suggests that NRF2 restrains IFN transcription.

Notably, FHIN1, but not DMF or MMF, increased IFNβ release from LPS-stimulated macrophages (Fig. 4b,c). This effect was independent of NAC-sensitive redox stress (Extended Data Fig. 8e) and was not due to augmented TLR4 signalling, as LPS-induced TRAF3 levels and IL-1β expression were not increased by FHIN1 (Extended Data Fig. 8f,g). FHIN1 and DMF modestly augmented LPS-induced p65 phosphorylation (Extended Data Fig. 8h), which may contribute to increased TNF release[42]. Given that FH inhibition causes mitochondrial stress (Fig. 2), which is associated with the release of immunostimulatory mitochondrial nucleic acids[43–45], we proposed that the IFN response is driven by cytosolic nucleic acid sensors, such as cGAS, RIG-I or MDA5. In support of this hypothesis, FH deficient-hereditary leiomyomatosis and renal cell cancer tumours exhibit changes in mitochondrial DNA (mtDNA)[21]. We first used ethidium bromide to deplete mtDNA[46] (Extended Data Fig. 8i) before treating cells with FHIN1 and LPS. FHIN1 no longer boosted LPS-induced IFNβ release in the presence of ethidium bromide (Fig. 4d), which indicated that the increased IFNβ release with FHIN1 may depend on mtDNA. We subsequently found that FHIN1 caused an increase in both mtDNA and mtRNA in cytosolic extracts (Fig. 4e and Extended Data Fig. 8j). Given the established role of mtDNA in driving IFN responses[43,44], we examined whether the cGAS–STING or TLR9

DNA-sensing pathways are required for the increase in IFNβ. However, treatment with the STING inhibitor C-178 (ref. [47]) or silencing of *Cgas* (which encodes cGAS) or *Tmem173* (which encodes STING) had no effect on FHIN1-driven IFNβ induction (Extended Data Fig. 8k–n). Targeting TLR9 using the competitive inhibitor ODN 2088 (ref. [48]) or using siRNA also had no effect on this response (Extended Data Fig. 8k–n). Suppression of *Tmem173* expression by FHIN1 or DMF (Extended Data Fig. 8o) may explain why cGAS–STING signalling is redundant in our model, even in the presence of cytosolic mtDNA. ETC inhibition, as observed with FHIN1 treatment, has also been shown to inhibit STING activation[49].

As cytosolic mtRNA was also increased by FHIN1 (Fig. 4e), we performed immunofluorescence staining with an antibody specific for double-stranded RNA (dsRNA). mtRNA has previously been shown to drive an IFN response in human cells[50,51], and is known to be particularly immunostimulatory[52]. FHIN1 treatment led to an accumulation of dsRNA relative to cells treated with dimethylsulfoxide (DMSO) as control (Fig. 4f). We subsequently treated cells with both FHIN1 and IMT1, an inhibitor of mitochondrial RNA polymerase (POLRMT). The increase in mtRNA following FHIN1 was observed in the cytosolic fraction but not in the whole cell fraction and was inhibited in both conditions with IMT1 treatment (Extended Data Fig. 8p,q). Notably, IMT1 also partly abrogated the FHIN1-mediated increase in IFNβ release (Extended Data Fig. 8r), which implies that mtRNA has a role in driving this response. Mitochondrial single-stranded RNA (ssRNA), which results from a decline in mitochondrial integrity, has also been implicated in driving TLR7-dependent IFN signalling[53,54]. We subsequently silenced *Tlr7* or the dsRNA sensors *Ddx58* (which encodes RIG-I) and *Ifih1* (which encodes MDA5) (Extended Data Fig. 9a,b), all of which abrogated the increase in IFNβ release observed with FH inhibition (Fig. 4g,h). This result confirms that there is a non-redundant requirement of these sensors and mtRNA, rather than mtDNA, for the FHIN1-driven IFN response. Knockdown of the cell surface dsRNA sensor *Tlr3* did not affect the augmentation in IFNβ release (Extended Data Fig. 9c). RIG-I and MDA5, although predominantly described as dsRNA sensors, can also bind ssRNA[55], which indicates that the IFN response following FH inhibition is probably driven by a mixture of dsRNA and ssRNA species. It is notable that FHIN1 also reduced *Ddx58* but not *Ifih1* expression, which may warrant further investigation (Extended Data Fig. 9b). The signalling events downstream of RIG-I–MDA5 activation include mitochondrial antiviral signalling protein (MAVS) oligomerization, followed by recruitment and phosphorylation of TANK-binding kinase 1 (TBK1). We observed MAVS oligomerization and increased TBK1 phosphorylation following FHIN1 treatment (Fig. 4i and Extended Data Fig. 9d). Notably, *Mavs* knockout did not impair the induction of IFNβ by FHIN1 (Extended Data Fig. 9e), which may indicate that compensatory TLR7 signalling is sufficient to drive type I IFN responses following FH inhibition with chronic MAVS deficiency.

We previously demonstrated that FH inhibition causes mitochondrial stress (Fig. 2). Changes in MMP have previously been correlated with increased type I IFN release[56]. Therefore we proposed that disturbances in MMP may be linked to mtRNA release and IFNβ induction following FH inhibition. To support this hypothesis, we induced changes in MMP by using the ATP synthase inhibitor oligomycin A, which increased MMP, the K^+ ionophore valinomycin A, which nonsignificantly reduced MMP, or the uncoupler CCCP, which

significantly dissipated MMP (Extended Data Fig. 9f,h). All treatments boosted LPS-driven IFNβ release, similar to effects with FHIN1 (Extended Data Fig. 9g,h). MMF, which does not increase LPS-induced IFNβ expression (Fig. 4c), did not affect MMP (Extended Data Fig. 9i). Oligomycin treatment led to an accumulation of dsRNA to a similar extent to that observed in cells treated with FHIN1 or transfected with dsRNA (poly(I:C)), and increased mtRNA release into the cytosol (Extended Data Fig. 9j–l). Valinomycin treatment similarly drove dsRNA accumulation (Extended Data Fig. 9m,n), which indicated that compounds that alter MMP induce an accumulation of mtRNA. As we also observed an increase in cytosolic mtDNA levels following oligomycin treatment (Extended Data Fig. 9l), it is still possible that IFN responses following oligomycin, valinomycin and CCCP treatment are not exclusively driven by mtRNA. mtRNA release from chondrocytes has recently been implicated in activating the immune response and promoting osteoarthritis[57]. As such, mitochondrial damage and nucleic acid release are emerging as key pathogenic processes that may underlie many immune-mediated diseases.

Tamoxifen-inducible *Fh1*^{-/-} BMDMs released more IFNβ after LPS stimulation than their *Fh1*^{+/+} counterparts (Fig. 4j). We also detected increased dsRNA accumulation in *Fh1*^{-/-} BMDMs (Fig 4k and Extended Data Fig. 9o), which, coupled with the fact that deletion of *Fh1* also drives mitochondrial membrane hyperpolarization (Fig. 2h), demonstrate that both genetic and pharmacological targeting of FH drive similar mitochondrial retrograde type I IFN stress responses.

We next considered whether this response could be applied to an endogenous model of LPS activation in the absence of pharmacological or genetic inactivation of FH. Given that LPS-induced FH suppression occurs predominantly during late-phase LPS stimulation (24–48 h) (Fig. 1g), FH suppression at this time point may drive membrane hyperpolarization and the release of mtRNA. MMP was significantly increased following 48 h of LPS stimulation, but not following 4 h or 24 h of stimulation (Extended Data Fig. 10a). Although dsRNA did not accumulate following acute (4 h) LPS stimulation (Extended Data Fig. 9j,k), we did observe increased dsRNA staining following 24 h and 48 h of LPS stimulation (Extended Data Fig. 10b,c). *Ddx58* and *Ifih1* expression is induced by LPS (Extended Data Fig. 10d), which suggests that RIG-I–MDA5 signalling is required during LPS stimulation. Indeed, silencing of *Ddx58* and *Ifih1* reduced *Ifnb1* expression induced by 24 h and 48 h of LPS stimulation (Fig. 4l). This result indicates that *Ifnb1* transcription during late-phase LPS stimulation is maintained by mtRNA release. These results demonstrate that the mitochondrial retrograde type I IFN response, which we initially unmasked by pharmacologically or genetically targeting FH during early LPS signalling, is active endogenously during late-phase LPS activation. These data have potential implications for chronic inflammation, for example, during ageing[58].

To determine whether FH inhibition leads to similar effects in vivo, we injected mice with FHIN1 or DMF before administration of LPS, and measured IFNβ release into the serum. FHIN1 increased LPS-induced IFNβ release, whereas DMF had no effect (Fig. 4m), which indicates that FH inhibition leads to a similar IFN response in vivo, which may have effects on bystander cells. We also treated human PBMCs with FHIN1 or DMF before

LPS stimulation and observed similar effects. That is, FHIN1 increased, whereas DMF suppressed, LPS-induced IFNβ release (Fig. 4n).

In summary, we described a mitochondrial retrograde signalling pathway leading from FH inhibition to mitochondrial membrane hyperpolarization and mtRNA release (Supplementary Fig. 1). Mitochondrial stress may be an underlying mechanism that contributes to type I IFN release in interferonopathies such as systemic lupus erythematosus (SLE). It has previously been demonstrated that PBMCs from patients with SLE have impaired mitochondrial function and altered MMP[59,60]. We therefore examined *FH* expression in the whole blood of patients with SLE and found significant suppression of *FH* compared with samples from healthy individuals (Fig. 4o). Autoantibodies to dsRNA, as well as dsDNA, have been detected in patients with SLE[61,62]. However, it is unclear whether FH suppression is a cause or consequence of increased IFN signalling, as *Fh1* can also be inhibited by IFNβ stimulation in BMDMs (Extended Data Fig. 10e). A negative feedback loop may exist whereby suppression of FH leads to type I IFN release, which feeds back to further suppress FH. FH suppression has also been previously linked to multiple sclerosis progression[63] and, in parallel to our work, has been shown to promote a type I IFN response in kidney epithelial cells and hereditary leiomyomatosis and renal cell cancer tumours (Zecchini et al. [64]). That study and ours implicate roles for FH in nucleic acid release, which may contribute to inflammation-driven tumorigenesis and as a potential host defence mechanism in the context of viral infection. Finally, a recent study[65] reported that aberrant dsRNA editing due to ADAR1 deficiency leads to MDA5 activation as a mechanism of common inflammatory diseases. Together, these data point to the clinical relevance of endogenously produced dsRNA and suggest that targeting this pathway may lead to new anti-inflammatory strategies.

Online content

Any methods, additional references, Nature Portfolio reporting summaries, source data, extended data, supplementary information, acknowledgements, peer review information; details of author contributions and competing interests; and statements of data and code availability are available at https://doi.org/10.1038/s41586-023-05720-6.

Methods

Animal details

All mice were on a C57BL/6JOlaHsd background unless stated below. Wild-type (WT) mice were bred in-house. The inducible $Fh1^{+/fl}$ and $Fh1^{fl/fl}$ mice were generated on the C57BL/6 genetic background, and their hind legs were donated by C. Frezza (University of Cambridge, UK). $Fh1^{+/+}$ and $Fh1^{-/fl}$ treated with vehicle (ethanol) were used as controls. Following treatment with 4-hydroxytamoxifen (TAM), Cre-mediated chromatin excision results in the loss of either one ($Fh1^{+/-}$) or both ($Fh1^{-/-}$) copies of *Fh1*, thus generating either heterozygous or null animals. Hind legs from WT and $Mavs^{-/-}$ mice were donated by C. Johansson (Imperial College London, UK). These strains, originally obtained from S. Akira (World Premier International Immunology Frontier Research Center, Osaka University, Osaka, Japan), were $Ifna6^{gfp/+}$, but since *Ifna6* expression was not a

primary readout, the mice are designated as WT and $Mavs^{-/-}$. In vitro experiments were performed with BMDMs isolated from 6–18-week-old female and male mice. Although we did not use statistical methods to calculate sample sizes, we decided to use a minimum of three biological replicates per experiment to account for biological variability, considering the three Rs principle (replacement, reduction and refinement) and the fact that most experiments were performed in primary macrophages from in-bred mice. All in vitro treatment groups were randomly assigned. In vitro and in vivo experiments were not blinded owing to the lack of available experimenters with required expertise. In vivo models were performed using 6-week-old male mice, and littermates were randomly assigned to experimental groups. Animals were maintained under specific pathogen-free conditions in line with Irish and European Union regulations. All animal procedures were approved by the Trinity College Dublin Animal Research Ethics Committee before experimentation and conformed with the Directive 2010/63/EU of the European Parliament.

Generation of mouse BMDMs

Mice (6–18 weeks old) were euthanized in a CO_2 chamber, and death was confirmed by cervical dislocation. Bone marrow was subsequently collected from the tibia, femur and ilium and cells were differentiated in DMEM containing L929 supernatant (20%), FCS (10%) and penicillin–streptomycin (1%) for 6 days, after which cells were counted and plated at 0.5×10^6 cells per ml unless otherwise stated. BMDMs were plated in 12-well cell culture plates and left overnight to adhere.

Isolation of human PBMCs

Human blood samples from healthy donors were collected and processed at the School of Biochemistry and Immunology at the Trinity Biomedical Sciences Institute (TCD). Blood samples were obtained anonymously, and written informed consent for the use of blood for research purposes was obtained from the donors. All the procedures involving experiments on human samples were approved by the School of Biochemistry and Immunology Research Ethics Committee (TCD). Experiments were conducted according to the TCD guide on good research practice, which follows the guidelines detailed in the National Institutes of Health Belmont Report (1978) and the Declaration of Helsinki. Whole blood (30 ml) was layered on 20 ml Lymphoprep (Axis-Shield), followed by centrifugation for 20 min at $400g$ with the brake off, after which the upper plasma layer was removed and discarded. The layer of mononuclear cells at the plasma-density gradient medium interface was retained, and 20 ml PBS was added. Cells were centrifuged for 8 min at $300g$ and the resulting supernatant was removed and discarded. The remaining pellet of mononuclear cells was resuspended, counted and plated at 1×10^6 cells per ml in RPMI supplemented with FCS (10%) and penicillin–streptomycin (1%).

Generation of human macrophages

PBMCs were obtained, and $CD14^+$ monocytes were isolated using a MagniSort Human CD14 Positive Selection kit (Thermo Fisher) according to the manufacturer's protocol. CD14 monocytes were then differentiated in T-175 flasks in RPMI containing FCS (10%), penicillin–streptomycin (1%) and recombinant human M-CSF (1:1,000). After 6 days, the supernatant was discarded, cells were scraped and counted, and human monocyte-derived

macrophages) were plated in 12-well plates at 1×10^6 cells per ml in RPMI containing FCS (10%) and penicillin–streptomycin (1%).

Whole blood isolation from patients with SLE

All patients with SLE (as per the diagnostic criteria of the American College of Rheumatology) were recruited from the Cedars–Sinai Medical Center. Age- and sex-matched healthy donors who had no history of autoimmune diseases or treatment with immunosuppressive agents were included. All participants provided informed written consent, and the study received approval from the institutional ethics review board (IRB protocol number 19627). Blood was collected into PAXgene RNA tubes (2.5 ml blood plus 6.9 ml buffer) and stored at –80 °C. Before isolation of RNA, the tubes were thawed at room temperature for 16 h. Total RNA was isolated using a PAXgene Blood RNA kit according to the manufacturer's recommendations (PreAnalytiX, 08/2005, 762174).

Reagents

LPS from *Escherichia coli*, serotype EH100 (ALX-581–010-L001), was purchased from Enzo Life Sciences. High molecular weight poly(I:C) (tlrl-pic) and $2'$–$3'$-cGAMP (tlrl-nacga23) were purchased from Invivogen. Recombinant mouse IFNβ1 (581302) and recombinant mouse IL-10 (417-ML-005/CF) were purchased from BioLegend. ATP disodium salt (A2383), DMSO (D8418), AOAA (C13408), valinomycin (V3639), TAM (H6278) and NAC (A7250) were purchased from Sigma Aldrich. Oligomycin A from *Streptomyces diastatochromogenes* (M02220) was purchased from Fluorochem. FHIN1 (HY-100004), DMF (HY-17363), MMF (HY-103252), IMT1 (HY-134539) and C-178 (HY-123963) were purchased from MedChemExpress. CPG ODN 1826 (130–100-274) and ODN 2088 (130–105-815) were purchased from Miltenyi Biotec. CCCP (M20036) was purchased from Thermo Fisher.

Compound treatments

All compounds used DMSO as a vehicle except for TAM (ethanol), NAC (PBS) and AOAA for tracing experiments (culture medium). LPS was used at a concentration of 100 ng ml^{-1} for indicated time points (2, 3, 4, 6, 8, 24 and 48 h). FHIN1 (10 or 20 μM), MMF (50 or 100 μM), DMF (25 μM), AOAA (5 mM), oligomycin (10 μM), CCCP (50 μM), NAC (1 mM) and IMT1 (10 μM) pre-treatments were performed for 3 h before the addition of LPS. Cells were treated with valinomycin (10 nM) 15 min before LPS stimulation. Anti-CD210 or IgG control (10 μg ml^{-1}) antibodies were added to cells 1 h before LPS stimulation. Recombinant mouse IL-10 protein (100 ng ml^{-1}) was added to cells at the same time as LPS. Cells were treated with IFNβ1 (220 ng ml^{-1}) for 3 h. Cells were treated with C-178 (1 μM) 1 h before LPS stimulation or transfection with $2'3'$-cGAMP (1.5 μg ml^{-1}) for 4 h to achieve cGAS–STING activation. Cells were treated with ODN 2088 (1 μM) for 1 h before LPS stimulation or transfection with CPG ODN 1826 (1.5 μg ml^{-1}) to achieve TLR9 activation. Three different time points of TAM (600 nM or 2 μM) or ethanol treatment were performed (specified in the individual figure legends). For 48-h treatments, ethanol and TAM were added on day 5 of 6 during the BMDM differentiation protocol. On day 6, they were plated with ethanol and TAM (left overnight) and treated the following day. For 72-h treatments, ethanol and TAM were added on day 4 of 6 during the BMDM differentiation

protocol. On day 6, they were plated with ethanol and TAM (left overnight) and treated the following day. For 96-h treatments, ethanol and TAM were added on day 4 of 6 during the BMDM differentiation protocol. On day 6, they were plated with ethanol and TAM and treated 2 days later.

Antibodies

Working dilutions of antibodies were 1:1,000 unless otherwise stated. Anti-mouse lamin B1 (12586), STAT1 (9172), p-STAT1 (9167), JAK1 (3344), p-JAK1 (3331), TBK1 (3504), p-TBK1 (5483), STAT3 (30835), p-STAT3 (9145), FH (4567), ASS1 (70720), α-tubulin (2144), α-tubulin (3873), MAVS (4983), ATF4 (11815), p-AKT (13038), AKT (2920), p-JNK (9255), JNK (9252), p-ERK1/2 (9101), ERK1/2 (4695), p-p38 (4511), p-38 (9212), TRAF3 (4729), p-p65 (3033) and GAPDH (2118) antibodies were purchased from Cell Signaling. Anti-goat IL-1β (AF-401-NA) was purchased from R&D. Anti-2SC antibody was provided by N. Frizzell (University of South Carolina, USA). Anti-mouse β-actin antibody (1:5,000) (A5316) was purchased from Sigma Aldrich. Horseradish peroxidase (HRP)-conjugated anti-mouse (115–035-003), anti-goat (705–035-003) and anti-rabbit (111–035-003) IgG antibodies (all 1:2,000) were purchased from Jackson Immunoresearch. Anti-mouse CD210 (112710) and anti-mouse IgG (406601) antibodies (both 10 μg ml^{-1}) were purchased from BioLegend. Anti-dsRNA antibody (clone rJ2, 1:60) was purchased from Merck (MABE-1134). Alexa Fluor 488 goat anti-mouse IgG1 antibody (A21121) was purchased from Invitrogen. Details of antibody validation are given in Supplementary Table 1.

RT–qPCR

RNA extraction from cells was carried out using a Purelink RNA kit (Invitrogen) according to the manufacturer's instructions. BMDMs were treated as required, and following treatment were instantly lysed in 350 μl RNA lysis buffer. Isolated RNA was quantified using a NanoDrop 2000 spectrophotometer, and RNA concentration was normalized to the lowest concentration across all samples with RNAse-free water. If necessary, samples were DNAse-treated after quantification using DNAse I (Thermo Fisher) according to the manufacturer's instructions. Isolated RNA samples were normalized and converted into cDNA using a High-Capacity cDNA Reverse Transcription kit (Thermo Fisher) according to the manufacturer's instructions. Next, 10 μl of RNA (at a maximum concentration of 100 ng μl^{-1}) was added to 10 μl of reverse transcription master mix to complete the reaction mixture. Real-time qPCR was performed on the cDNA generated in the previous step, using primers designed in-house and ordered from Eurofins Genomics, as detailed in Supplementary Table 2. The reaction was performed in a 96-well qPCR plate using a 7500 Fast Real-Time PCR machine (Thermo Fisher). Relative expression ($2^{-\Delta C_T}$) was calculated from the C_T values for each sample and gene of interest.

RNA interference

Pre-designed silencer select siRNAs for *Cgas* (s103166), *Tmem173* (s91058), *Tlr3* (s100579), *Tlr9* (s96268), *Asl* (s99640), *Tlr7* (s100720), *Ddx58* (s106376), *Ifih1* (s89787), *Nrf2* (s70522), *Atf4* (s62689) and negative control (4390843) were ordered from Thermo Fisher. siRNA sequences are given in Supplementary Table 2. Cells were transfected with

50 nM siRNA using 5 µl Lipofectamine RNAiMAX according to the manufacturer's instructions (Thermo Fisher). Cells were transfected in medium without serum and antibiotics, which was replaced with complete medium 8 h later. Cells were subsequently left for at least a further 12 h before treatment.

Immunofluorescence

Cells were plated on 20 mm cover slips in 12-well plates. Cells were treated as required and Mitotracker Red CMXRos (100 nM, Thermo Fisher) was added to medium 30 min before the end of cell treatments. After 30 min of incubation, cells were washed three times with warm PBS. Cells were subsequently fixed for 10 min with 4% paraformaldehyde in PBS at 37 °C. Cells were washed three times with PBS and permeabilized for 1 h in block solution (1% BSA, 22.52 mg ml^{-1} glycine and 0.1% Tween 20 in PBS). Anti-dsRNA antibody (Merck) was diluted 1:60 in block solution and incubated with cells overnight at room temperature. Cells were washed three times with PBS for 5 min per wash. A mix containing AF488-conjugated goat anti-mouse IgG1 antibody (1:1,000) and DAPI (1:1,000, Thermo Fisher) was subsequently added to cells for 90 min at room temperature in the dark. Cells were subsequently washed three times with PBS for 5 min per wash. Cover slips were mounted onto microscope slides using 10–20 µl ProLong Gold antifade reagent (Thermo Fisher). Slides were imaged using a Leica SP8 scanning confocal microscope with a ×20.0 objective. Images were analysed using LAS X Life Science Microscope Software Platform (Leica). The same microscope instrument settings were used for all samples, and all images were analysed using the same settings. Quantification of dsRNA or Mitotracker Red CMXRos signal intensity was performed using the measure function in ImageJ 1.53t (NIH). The mean signal intensity was calculated for individual cells in single colour images and displayed relative to signal intensity of control cells.

Flow cytometry

Cells were plated in 12-well plates and treated as desired. CellROX Green (5 µM, Thermo Fisher) or TMRM (20 nM, Thermo Fisher) was added to cells 30 min before the end of cell treatments. Cells were washed once in PBS and scraped into 200 µl FACS buffer (2 mM EDTA and 0.5% FCS in PBS). Acquisition of samples was performed using a BD Accuri C6 flow cytometer. The gating strategy used for all flow cytometry experiments consisted of debris exclusion by FSC-A versus SSC-A analysis and subsequent doublet exclusion by FSC-A versus FSC-H analysis. A sample gating strategy is provided in Supplementary Fig. 2. Overall, 10,000 cells were acquired per condition. The mean fluorescence intensity (MFI) was calculated for all cells in each condition using FlowJo v.10.

Liquid chromatography–mass spectrometry

Steady-state metabolomics.—BMDMs (3 independent mice) were plated at 0.5×10^6 cells per well in 12-well plates in technical triplicate per condition, treated as indicated, snap frozen and stored at −80 °C. For metabolomics of the cytosolic fraction, BMDMs were plated at 10×10^6 cells per 10 cm dish, and rapid fractionation was performed as previously reported[16]. Metabolite extraction solution (methanol:acetonitrile:water, 50:30:20 v/v/v) was added (0.5 ml per 1×10^6 cells), and samples were incubated for 15 min on

dry ice. The resulting suspension was transferred to ice-cold microcentrifuge tubes. Samples were agitated for 20 min at 4 °C in a thermomixer and then incubated at −20 °C for 1 h. Samples were centrifuged at maximum speed for 10 min at 4 °C. The supernatant was transferred into a new tube and centrifuged again at maximum speed for 10 min at 4 °C. The supernatant was transferred to autosampler vials and stored at −80 °C before analysis by liquid chromatography–mass spectrometry (LC–MS).

HILIC chromatographic separation of metabolites was achieved using a Millipore Sequant ZIC-pHILIC analytical column (5 μm, 2.1 × 150 mm) equipped with a 2.1 × 20 mm guard column (both 5 mm particle size) with a binary solvent system. Solvent A was 20 mM ammonium carbonate and 0.05% ammonium hydroxide; solvent B was acetonitrile. The column oven and autosampler tray were held at 40 °C and 4 °C, respectively. The chromatographic gradient was run at a flow rate of 0.200 ml min^{-1} as follows: 0–2 min: 80% solvent B; 2–17 min: linear gradient from 80% solvent B to 20% solvent B; 17–17.1 min: linear gradient from 20% solvent B to 80% solvent B; 17.1–22.5 min: hold at 80% solvent B. Samples were randomized and analysed by LC–MS in a blinded manner, and the injection volume was 5 μl. Pooled samples were generated from an equal mixture of all individual samples and analysed interspersed at regular intervals within a sample sequence as a quality control. Metabolites were measured with a Thermo Scientific Q Exactive Hybrid Quadrupole-Orbitrap mass spectrometer coupled to a Dionex Ultimate 3000 UHPLC or with Vanquish Horizon UHPLC coupled to an Orbitrap Exploris 240 mass spectrometer (both Thermo Fisher Scientific) through a heated electrospray ionization source.

For the Thermo Scientific Q Exactive Hybrid Quadrupole-Orbitrap Mass spectrometer (HRMS) coupled to a Dionex Ultimate 3000 UHPLC, the mass spectrometer was operated in full-scan, polarity-switching mode, with the spray voltage set to +4.5 kV/−3.5 kV, the heated capillary held at 280 °C and the heated electrospray ionization probe held at 320 °C. The sheath gas flow was set to 40 units, the auxiliary gas flow was set to 15 units and the sweep gas flow was set to 0 unit. HRMS data acquisition was performed in a range of m/z = 70–900, with the resolution set at 70,000, the AGC target at 1 × 10^6 and the maximum injection time (max IT) at 120 ms. Metabolite identities were confirmed using two parameters: (1) precursor ion m/z was matched within 5 ppm of theoretical mass predicted by the chemical formula; (2) the retention time of metabolites was within 5% of the retention time of a purified standard run with the same chromatographic method. Chromatogram review and peak area integration were performed using the Thermo Fisher software XCalibur Qual Browser, XCalibur Quan Browser software and Tracefinder 5.0. The peak area for each detected metabolite was normalized against the total ion count of that sample to correct any variations introduced from sample handling through instrument analysis. Absolute quantification of 2SC was performed by interpolation of the corresponding standard curve obtained from serial dilutions of commercially available standards (Sigma Aldrich) running with the same batch of samples.

For the Orbitrap Exploris 240 mass spectrometer, MS1 scans, the mass range was set to m/z = 70–900, AGC target set to standard and maximum injection time (IT) set to auto. Data acquisition for experimental samples used full scan mode with polarity switching at an Orbitrap resolution of 120,000. Data acquisition for untargeted metabolite identification was

performed using the AcquireX Deep Scan workflow, an iterative data-dependent acquisition strategy using multiple injections of the pooled sample. In brief, the sample was first injected in full scan-only mode in single polarity to create an automated inclusion list. MS2 acquisition was then carried out in triplicate, whereby ions on the inclusion list were prioritized for fragmentation in each run, after which both the exclusion and inclusion lists were updated in a manner such that fragmented ions from the inclusion list were moved to the exclusion list for the next run. Data-dependent acquisition full-scan ddMS2 method for AcquireX workflow used the following parameters: full scan resolution was set to 60,000, fragmentation resolution to 30,000 and fragmentation intensity threshold to 5.0×10^3. Dynamic exclusion was enabled after 1 time and exclusion duration was 10 s. Mass tolerance was set to 5 ppm. The isolation window was set to 1.2 m/z. Normalized HCD collision energies were set to stepped mode with values at 30, 50 and 150. Fragmentation scan range was set to auto, AGC target at standard and max IT at auto. Xcalibur AcquireX method modification was on. Mild trapping was enabled.

Metabolite identification was performed using the Compound Discoverer software (v.3.2, Thermo Fisher Scientific). Metabolites were annotated at the MS2 level using both an in-house mzVault spectral database curated from 1,051 authentic compound standards and the online spectral library mzCloud. The precursor mass tolerance was set to 5 ppm and fragment mass tolerance set to 10 ppm. Only metabolites with mzVault or mzCloud best match score above 50% and 75%, respectively, and retention time tolerance within 0.5 min to that of a purified standard run with the same chromatographic method were exported to generate a list including compound names, molecular formula and retention time. The curated list was then used for further processing in the Tracefinder software (v.5.0, Thermo Fisher Scientific), in which extracted ion chromatographs for all compounds were examined and manually integrated if necessary. False positive, noise or chromatographically unresolved compounds were removed. The peak area for each detected metabolite was then normalized against the total ion count of that sample to correct any variations introduced from sample handling through instrument analysis. The normalized areas were used as variables for further statistical data analysis. Statistical analysis was performed using MetaboAnalyst (v.5.0)[66].

Stable isotope-assisted tracing.—BMDMs (3 independent mice) were plated at 0.5 $\times 10^6$ cells per well in 12-well plates in technical triplicate per condition and treated as indicated in glutamine-free DMEM supplemented with U-^{13}C-glutamine or ^{15}N$_2$-glutamine, respectively. For ^{13}C- and ^{15}N-tracing analysis, the theoretical masses of ^{13}C and ^{15}N isotopes were calculated and added to a library of predicted isotopes in Tracefinder 5.0. These masses were then searched with a 5 ppm tolerance and integrated only if the peak apex showed less than 1% deviation in retention time from the [U-^{12}C or ^{14}N] monoisotopic mass in the same chromatogram. The raw data obtained for each isotopologue were corrected for natural isotope abundances using the AccuCor algorithm (https://github.com/lparsons/accucor) before further statistical analysis.

Ethidium bromide treatment

BMDMs were plated in the presence or absence of ultrapure ethidium bromide (100 ng ml^{-1}) and incubated for a further 6 days before treatment. Depletion of mtDNA was determined by genomic DNA isolation followed by qPCR using primers specific for areas of mitochondrial DNA (D-loop) and areas of mtDNA that are not inserted into nuclear DNA (non-NUMT).

c-Fos activity assay

BMDMs from 3 mice were plated in 10 cm dishes at 0.5×10^6 cells per ml and left overnight. Cells were pre-treated with FHIN1 or DMF (3 h) before LPS stimulation (4 h). After collection, nuclear extracts were isolated using a Nuclear Extraction kit (ab113474) purchased from Abcam. Nuclear extracts were quantified using a BCA assay and standardized. c-Fos relative activity was then quantified using the AP-1 transcription factor assay purchased from Abcam (Ab207196) according to the manufacturer's protocol.

Fumarate assay

Analysis of fumarate levels were assessed using a fumarate colorimetric assay kit (Sigma MAK060) that uses an enzyme assay, which results in a colorimetric (450 nm) product proportional to the fumarate present, as per the manufacturer's instructions.

Nitrite measurement

The Griess reagent system (Promega G2930) was used according to the manufacturer's instructions.

RNA-seq

BMDMs (three independent mice) were treated as indicated and RNA was extracted as detailed above. mRNA was extracted from total RNA using poly-T-oligo-attached magnetic beads. After fragmentation, the first strand cDNA was synthesized using random hexamer primers, followed by the second strand cDNA synthesis. The library was checked using Qubit and real-time PCR for quantification and a bioanalyser for size distribution detection. Quantified libraries were pooled and sequenced on a NovaSeq 6000 S4 (Illumina). Differential expression analysis of two conditions per group was performed using counted reads and the DESeq2 R package[67]. Pathway enrichment analyses were performed as indicated in quantification and statistical analysis section below.

Proteomic analysis

Sample preparation.—BMDMs (from five independent mice) were plated onto 10 cm dishes and treated as indicated. At the experimental end point, cells were washed with PBS on ice and centrifuged at 1,500 r.p.m. for 5 min at 4 °C and frozen at −80 °C. Cell pellets were lysed, reduced and alkylated in 50 μl of 6 M Gu-HCl, 200 mM Tris-HCl pH 8.5, 10 mM TCEP, 15 mM chloroacetamide by probe sonication and heating to 95 °C for 5 min. Protein concentration was measured using a Bradford assay and initially digested with LysC (Wako) with an enzyme/substrate ratio of 1:200 for 4 h at 37 °C. Subsequently, the samples were diluted tenfold with water and digested with porcine trypsin (Promega) at 37 °C

overnight. Samples were acidified to 1% TFA, cleared by centrifugation (16,000g at room temperature) and approximately 20 μg of the sample was desalted using a Stage-tip. Eluted peptides were lyophilized, resuspended in 0.1% TFA/water and the peptide concentration was measured by A280 on a nanodrop instrument (Thermo). The sample was diluted to 2 μg in 5 μl for subsequent analysis.

Mass spectrometry analysis.—The tryptic peptides were analysed using a Fusion Lumos mass spectrometer connected to an Ultimate Ultra3000 chromatography system (both Thermo Scientific) incorporating an autosampler. In brief, 2 μg of de-salted peptides were loaded onto a 50 cm emitter packed with 1.9 μm ReproSil-Pur 200 C18-AQ (Dr Maisch) using a RSLC-nano uHPLC system connected to a Fusion Lumos mass spectrometer (both Thermo). Peptides were separated using a 140 min linear gradient from 5% to 30% acetonitrile, 0.5% acetic acid. The mass spectrometer was operated in DIA mode, acquiring a MS 350–1,650 Da at 120 k resolution followed by MS/MS on 45 windows with 0.5 Da overlap (200–2,000 Da) at 30 k with a NCE setting of 27.

Data analysis.—Raw files were analysed and quantified by searching against the UniProt *Mus musculus* database using DIA-NN 1.8 (https://github.com/vdemichev/DiaNN). Library-free search was selected, and the precursor ion spectra were generated from the FASTA file using the deep-learning option. Default settings were used throughout apart from using 'Robust LC (high precision)'. In brief, carbamidomethylation was specified as the fixed modification whereas acetylation of protein amino termini was specified as the variable. Peptide length was set to a minimum of 7 amino acids, precursor false discovery rate (FDR) was set to 1%. Subsequently, missing values were replaced by a normal distribution (1.8 π shifted with a distribution of 0.3 π) to allow the following statistical analysis. Protein-wise linear models combined with empirical Bayes statistics were used for the differential expression analyses. We use the Bioconductor package limma to carry out the analysis using the information provided in the experimental design table.

Digitonin fractionation

BMDMs were plated at 0.5×10^6 cells per well and treated as desired. After treatment, cells were washed once with room temperature PBS before being scraped on ice into ice-cold PBS and pelleted at 500g for 5 min at 4 °C. Supernatant was removed and discarded, and the pellet was resuspended in 400 μl extraction buffer (150 mM NaCl, 50 mM HEPES pH 7.4, and 25 μg ml^{-1} digitonin). Samples were then placed in a rotating mixer at 4 °C for 10 min before centrifugation at 2,000g at 4 °C for 5 min. The resulting supernatant constituted the cytosolic fraction, from which RNA and DNA were isolated using an AllPrep DNA/ RNA Mini kit (Qiagen). Alternatively, the cytosolic fraction was concentrated using Strataclean resin (Agilent) and analysed by western blotting. The pellet constituted a fraction containing membrane-bound organelles, which was lysed in RNA lysis buffer for RNA isolation or lysed in western blot lysis buffer for analysis by western blotting. To determine the presence of mtRNA and mtDNA in the cytosol, qPCR was performed using primers specific for mitochondrial D-loop on cDNA, which had been reverse-transcribed from RNA isolated from the cytosolic fraction (mtRNA) and on DNA isolated from the cytosolic fraction (mtDNA). In both cases, values were normalized using a housekeeping control gene (*Actb*,

which encodes β-actin) amplified in cDNA, which had been reverse-transcribed from RNA isolated from the membrane-bound fraction.

MAVS oligomerization

BMDMs were plated at 1×10^6 cells per well in technical triplicate and treated as desired. After treatment, cells were washed twice with 200 μl cold PBS before being lysed in crosslinking lysis buffer (50 mM HEPES, 0.5% Triton X-100 and 1× protease inhibitor cocktail). Samples were placed on ice for 15 min. Lysates were centrifuged for 15 min at 6,000g at 4 °C and the supernatant was removed and frozen down as the soluble fraction. Next, 20 μl of the soluble fraction was mixed with 5 μl of sample lysis buffer (0.125 M Tris pH 6.8, 10% glycerol, 0.02% SDS and 5% DTT) and run on a 10% gel. The insoluble pellet was resuspended in HEPES (50 mM) and washed 3 times by centrifuging at 6,000g at 4 °C and removing the supernatant each time. After the final wash, the pellet was resuspended in 500 μl crosslinking buffer (50 mM HEPES and 150 mM NaCl) and disuccinimidyl suberate (Thermo Fisher, made up in anhydrous DMSO) was added to the final concentration of 2 mM. Immediately following the addition of disuccinimidyl suberate, the sample was inverted several times and incubated for 45 min at 37 °C. The sample was then centrifuged for 15 min at 6,000g at 4 °C, before the supernatant was removed and the pellet was resuspended in 30 μl sample lysis buffer. The resuspended insoluble fraction was subsequently boiled for 5 mins at 95 °C before being run on a gel.

Seahorse XF glycolysis stress test

Cells were plated at 100,000 cells per well in 100 μl and were left overnight to adhere. The protocol was carried out according to the manufacturer's instructions (Agilent). In brief, cells were treated as required, after which the medium was replaced with Seahorse medium containing glutamine (2 mM). Cells were then placed in a CO_2-free incubator for 1 h. The glycolysis stress test was subsequently performed using a Seahorse XFe96 analyzer (Agilent) with the following injections: glucose (10 mM); oligomycin (1 μM); and 2-DG (50 mM).

Analysis was performed using Seahorse Wave software (Agilent). Data shown are representative experiments containing at least three pooled biological replicates.

Seahorse XF mito stress test

Cells were plated at 100,000 cells per well in 100 μl and were left overnight to adhere. The protocol was carried out according to manufacturer's instructions (Agilent). In brief, cells were treated as required, after which the medium was replaced with Seahorse medium containing glutamine (2 mM), glucose (10 mM) and pyruvate (1 mM). Cells were then placed in a CO_2-free incubator for 1 h. The mito stress test was subsequently performed using a Seahorse XFe96 analyzer (Agilent) with the following injections: oligomycin (1 μM); FCCP (1 μM); and rotenone (500 nM)

Analysis was performed using Seahorse Wave software (Agilent). Data shown are representative experiments containing at least three pooled biological replicates.

LPS-induced inflammation model

Male mice (6 weeks old) were used, and littermates were randomly assigned to experimental groups. Compounds were resuspended in 10% DMSO followed by 90% cyclodextrin in PBS (20% w/v). Mice were intraperitoneally injected with vehicle, FHIN1 or DMF (both 50 mg kg^{-1}) at a volume of 200 μl per injection. After 1 h, mice were intraperitoneally injected with PBS or LPS from *E. coli* (2.5 mg kg^{-1}, Sigma) at a volume of 100 μl per injection. After 2 h, mice were euthanized and blood was collected retro-orbitally. Blood was allowed to clot for 30 min at room temperature before it was centrifuged at 5,000*g* for 10 min at 4 °C. The serum was removed and the IFNβ concentration was determined by ELISA.

Western blotting

Supernatant was removed from cells following stimulation, and lysates were collected in 30–50 μl lysis buffer (0.125 M Tris pH 6.8, 10% glycerol, 0.02% SDS and 5% DTT) Lysates were subsequently heated to 95 °C for 5 min to denature proteins. SDS–PAGE was used to resolve proteins by molecular weight. Samples were boiled at 95 °C for 5 min before loading into a 5% stacking gel. The percentage resolving gel depended on the molecular weight of the given protein. The Bio-Rad gel running system was used to resolve proteins, and the Bio-Rad wet transfer system was used for the electrophoretic transfer of proteins onto a PVDF membrane. Following transfer, the membrane was incubated in milk powder (5% in TBST) for 1 h and subsequently incubated in primary antibody rolling overnight at 4 °C. Primary antibodies targeting phospho-proteins were diluted in BSA (5% in TBST) as opposed to milk. The membrane was incubated for 1 h with secondary antibody (diluted in 5% milk powder) at room temperature. Before visualization, the membrane was immersed in WesternBright ECL Spray (Advansta). Protein visualization was performed using a ChemiDoc MPTM imaging system (Bio-Rad), and both chemiluminescent and white light images were taken. Images were analysed using Image Lab 6.0.1 (Bio-Rad).

ELISA.—DuoSet ELISA kits for IL-1β, TNF, IL-6, IL-10 and GDF15 were purchased from R&D Systems and were carried out according to the manufacturer's instructions with appropriately diluted cell supernatants added to each plate in duplicate or triplicate. IFNβ was determined using a DuoSet ELISA kit from R&D Systems or Abcam (ab252363). Quantikine ELISA kit for IFNβ (R&D Systems) was used for determination of IFNβ concentrations in serum samples and from human cells, and these were also carried out according to the manufacturer's instructions. Absorbance at 450 nm was quantified using a FLUOstar Optima plate reader. Corrected absorbance values were calculated by subtracting the background absorbance, and cytokine concentrations were subsequently obtained by extrapolation from a standard curve plotted using GraphPad Prism 9.2.0.

Quantification and statistical analyses

Details of all statistical analyses performed are provided in the figure legends. Data are expressed as the mean ± s.e.m. unless stated otherwise. Representative western blots are shown. For metabolomics data, MetaboAnalyst (v.5.0)[66] was used to analyse, perform statistics and visualize the results. Autoscaling of features (metabolites) was used for heatmap generation. One-way analysis of variance (ANOVA) corrected for multiple

comparisons using the Tukey statistical test was used, and a P-adjusted < 0.05 was set as the cut-off. For proteomics data, protein signal intensity was converted to a $\log_2$ scale, and biological replicates were grouped by experimental condition. Protein-wise linear models combined with empirical Bayes statistics were used for the differential expression analyses. The Bioconductor package limma was used to carry out the analysis using a R-based online tool[68]. Data were visualized using a heatmap with autoscaled features (genes) and a volcano plot, which shows the $\log_2$(fold change) on the x axis and the $-\log_{10}$(adjusted P value) on the y axis. The proteomics cut-off values for analysis were a $\log_2$(fold change) of 0.5 and a FDR < 0.05, which were determined using t-statistics. RNA-seq cut-off values were set to $\log_2$(fold change) of 1 and FDR < 0.05. Overrepresentation analysis of significant changes were assessed using Enrichr and the Bioconductor package clusterProfiler 4.0 in R (v.3.6.1). Further information on this visualization method is available[69]. Emapplots were generated using the enrichplot package in R (v.3.6.1). GSEA analysis of RNA-seq was performed using the Broad Institutes GSEA (v.4.1.0)[70]. Graphpad Prism v.9.2.0 was used to calculate statistics in bar plots using appropriate statistical tests depending on the data, including one-way ANOVA, two-tailed unpaired t-test and multiple t-tests. Adjusted P values were assessed using appropriate correction methods, such as Tukey, Kruskal–Wallis and Holm–Sidak tests. Sample sizes were determined on the basis of previous experiments using similar methodologies. All depicted data points are biological replicates taken from distinct samples unless stated otherwise. Each figure consists of a minimum of three independent experiments from multiple biological replicates unless stated otherwise. For in vivo studies, mice were randomly assigned to treatment groups. For metabolomics, proteomics and RNA-seq analyses, samples were processed in random order and experimenters were blinded to experimental conditions.

Reporting summary

Further information on research design is available in the Nature Portfolio Reporting Summary linked to this article.

Data availability

Proteomics data from Fig. 1d were previously deposited[11] to the ProteomeXchange Consortium through the PRIDE partner repository with the dataset identifier PXD029155. All other proteomics, RNA-seq data and metabolomics data have been deposited to Dryad (https://doi.org/10.5061/dryad.6wwpzgn28). All other data are available from the corresponding authors upon request. Source data are provided with this paper.
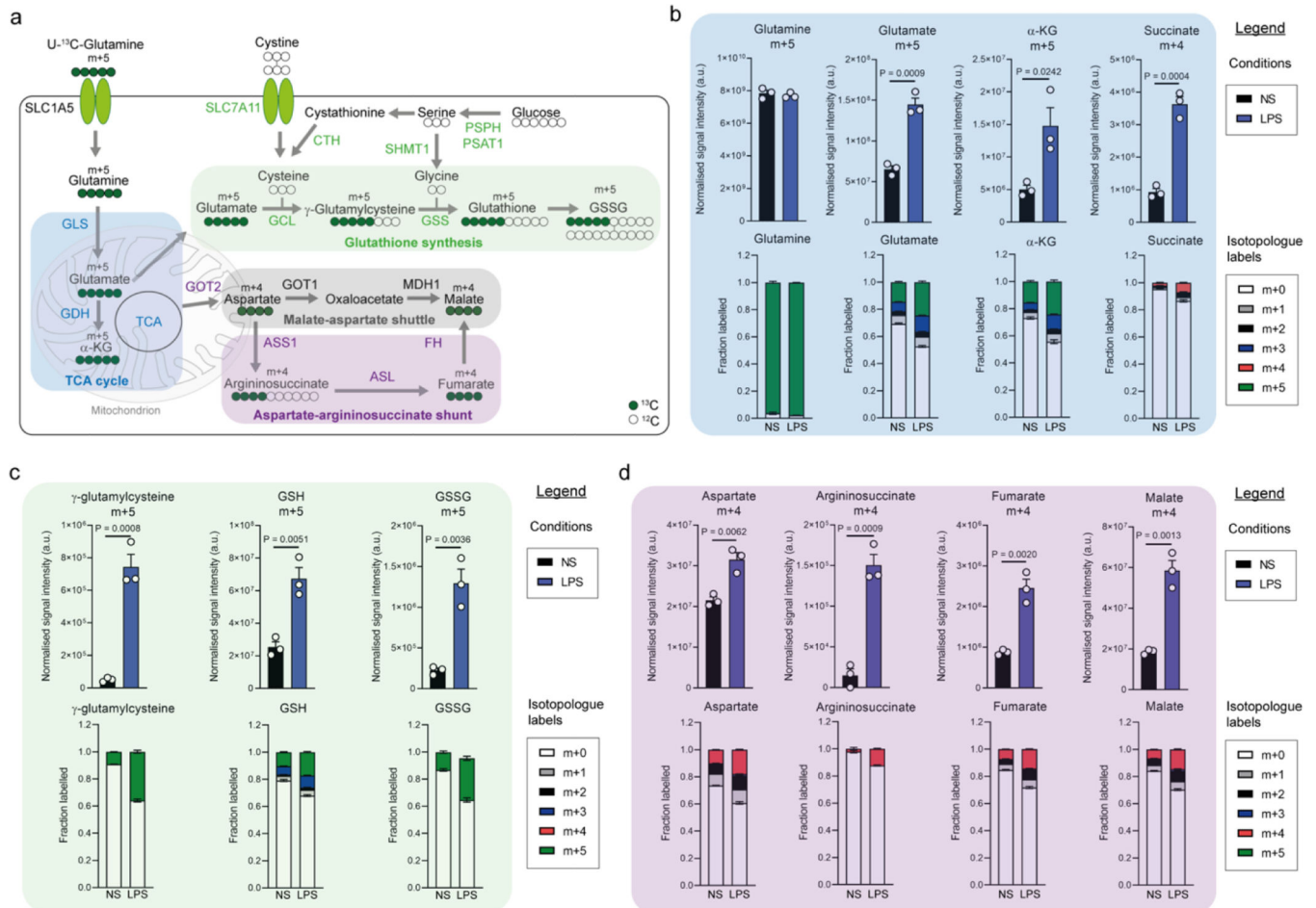
Extended Data
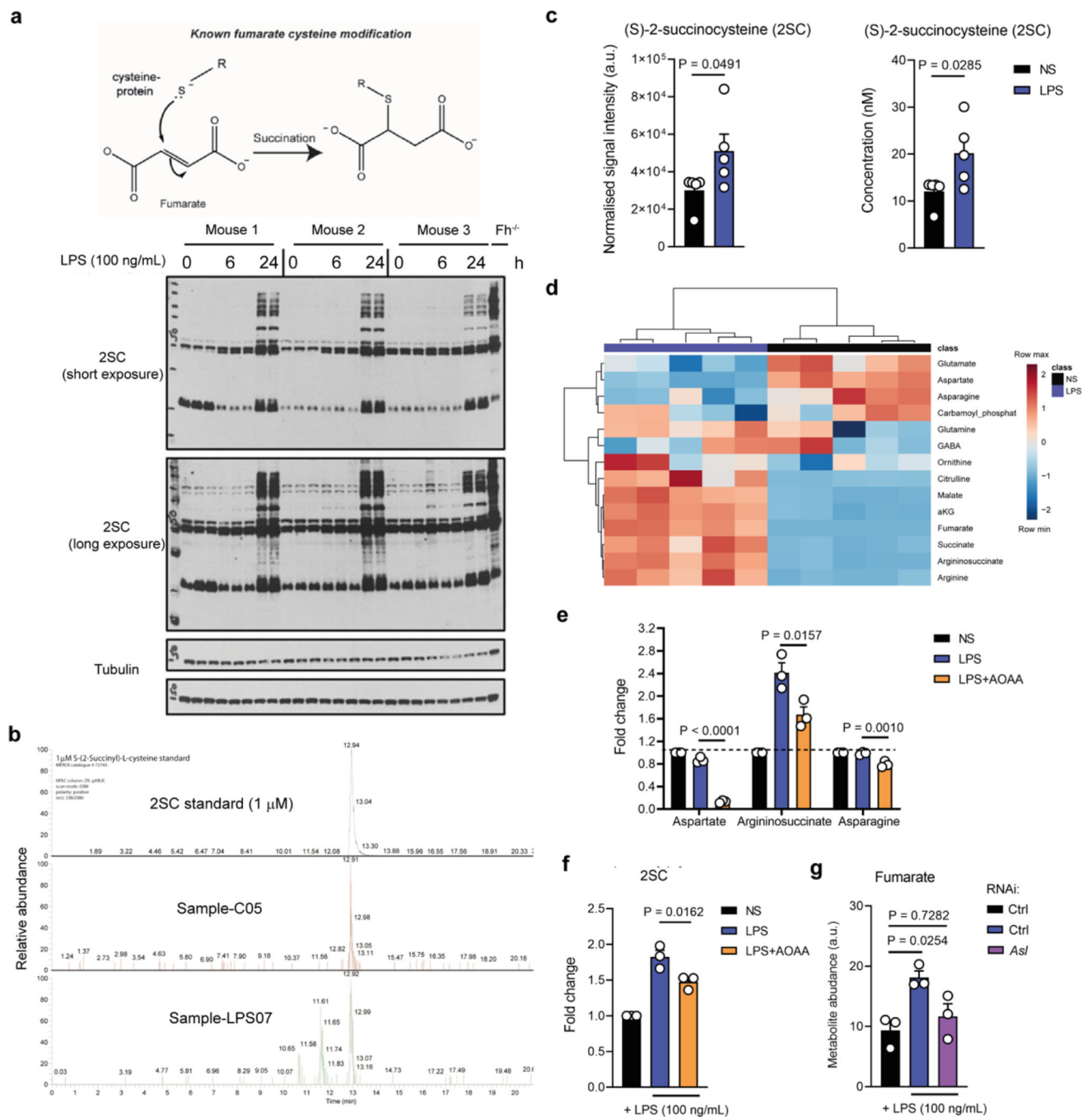
Extended Data Figure 1 –. LPS stimulation drives fumarate accumulation and protein succination

a-c, Fumarate-mediated protein succination with LPS ($n = 3$) and 2SC abundance in NS and LPS-stimulated mouse macrophages ($n = 5$; LPS 4 h). **d,** Heatmap of metabolites linked to aspartate-argininosuccinate shunt in NS and LPS-stimulated mouse macrophages ($n = 5$; LPS 24 h) **e,** Metabolite abundance of aspartate-argininosuccinate shunt metabolites in LPS-stimulated mouse macrophages pre-treated with DMSO or AOAA ($n = 3$; LPS 4 h).

f, 2SC levels following LPS stimulation with or without AOAA pre-treatment (3 h) ($n = 3$; LPS 4 h). **c,e-g,** Data are mean ± s.e.m. **a,** Representative blots shown. *P* values calculated using two-tailed Student's *t*-test for paired comparisons or one-way ANOVA for multiple comparisons.


Extended Data Figure 2 –. LPS stimulation drives fumarate accumulation via glutamine anaplerosis and an aspartate-argininosuccinate shunt

a, Schematic diagram indicating U-^{13}C-glutamine tracing into distinct metabolic nodules.

b, U-^{13}C-glutamine tracing into glutamate, α-KG and succinate in LPS-treated mouse macrophages (m+4 and m+5 labelling intensity and total isotopologue fraction distribution) ($n = 3$; LPS 4 h). **c,** U-^{13}C-glutamine tracing into γ-glutamylcysteine, GSH and GSSG in LPS-treated mouse macrophages (m+5 labelling intensity and total isotopologue fraction distribution) ($n = 3$; LPS 4 h). **d,** U-^{13}C-glutamine tracing into aspartate, argininosuccinate, fumarate and malate in LPS-treated mouse macrophages (m+4 and m+5 labelling intensity and total isotopologue fraction distribution) ($n = 3$; LPS 4 h). Data are mean ± s.e.m. *P* values calculated using two-tailed Student's t-test for paired comparisons.
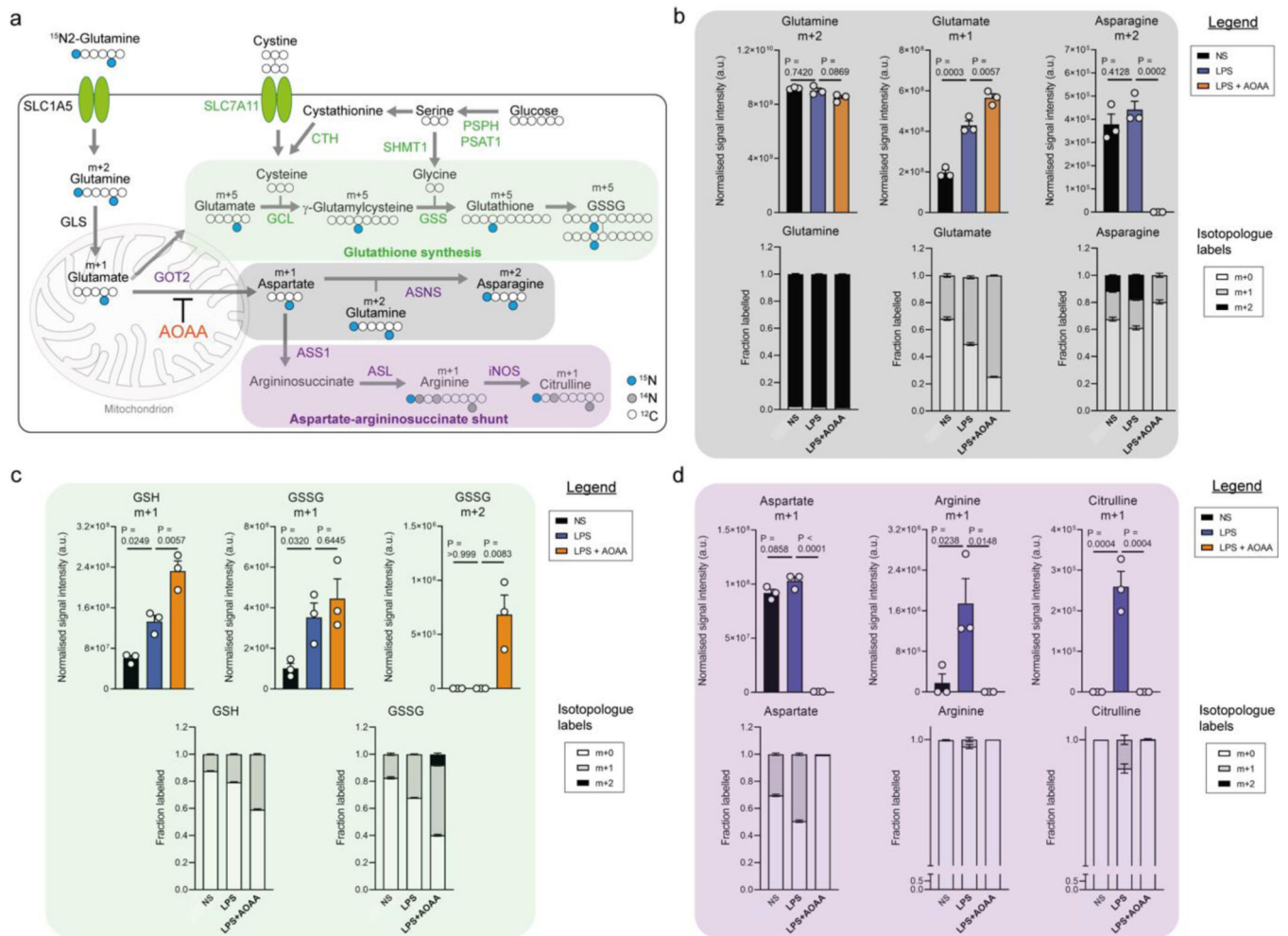
Extended Data Figure 3 –. LPS stimulation drives fumarate accumulation via glutamine anaplerosis and an aspartate-argininosuccinate shunt

a, Schematic diagram indicating $^{15}N_2$-glutamine tracing into distinct metabolic nodules. **b,** $^{15}N_2$-glutamine tracing into glutamate and asparagine in LPS-treated mouse macrophages (m+1 and m+2 labelling intensity and total isotopologue fraction distribution) ($n = 3$; LPS 4 h). **c,** $^{15}N_2$-glutamine tracing into GSH and GSSG in LPS-treated mouse macrophages (m+1 and m+2 labelling intensity and total isotopologue fraction distribution) ($n = 3$; LPS 4 h). **d,** $^{15}N_2$-glutamine tracing into aspartate, arginine and citrulline in LPS-treated mouse macrophages (m+1 labelling intensity and total isotopologue fraction distribution) ($n = 3$; LPS 4 h). Data are mean ± s.e.m. *P* values calculated using one-way ANOVA for multiple comparisons.
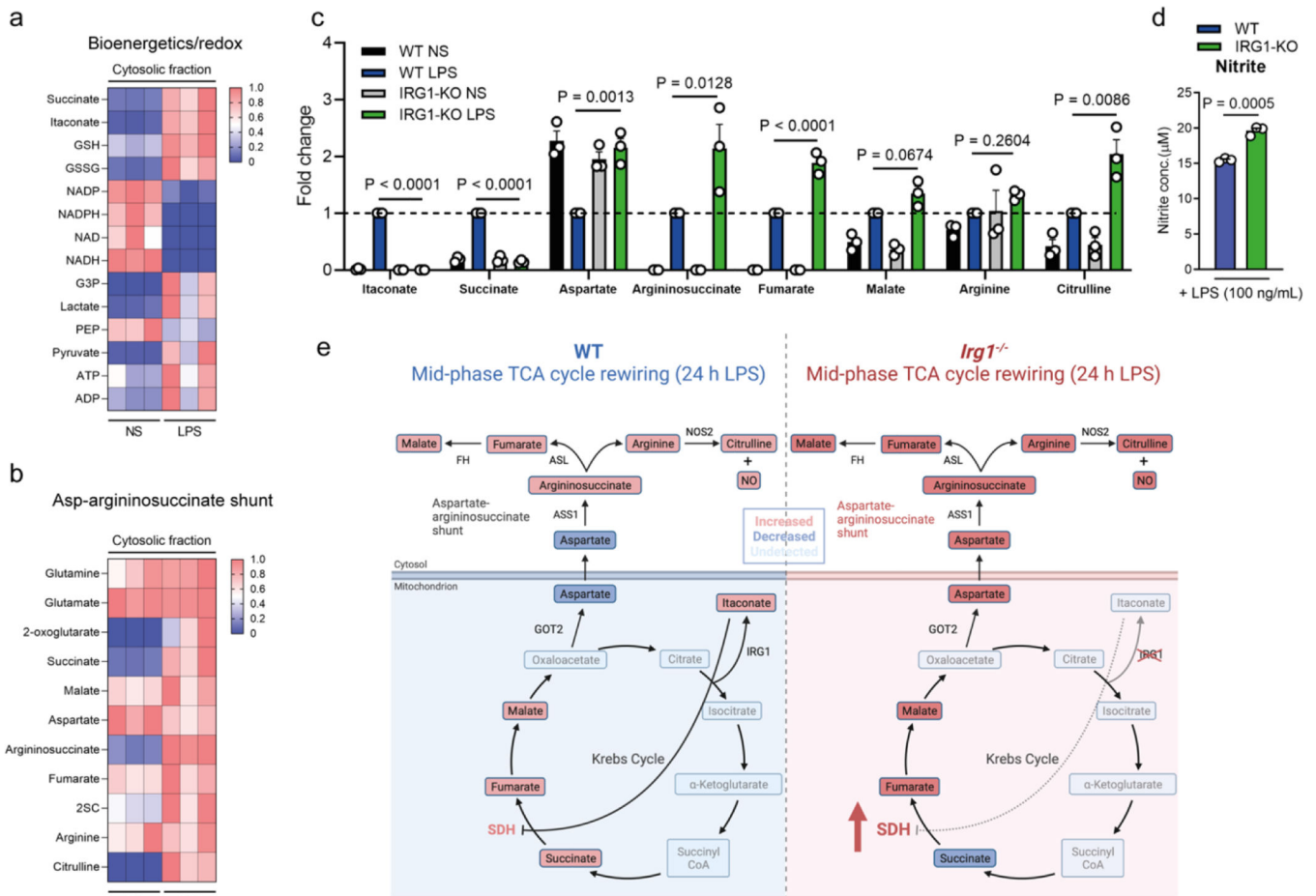
Extended Data Figure 4 –. Increase in aspartate-argininosuccinate shunt metabolites in cytosol and *Irg1*^{−/−} macrophages

Heatmap (min-max) of metabolites linked to mitochondrial bioenergetics and redox signalling (**a**) and the aspartate-argininosuccinate shunt (**b**) in NS and LPS-stimulated mouse macrophages ($n = 3$; LPS 24 h). **c,** Metabolite abundance of TCA cycle and aspartate-argininosuccinate shunt metabolites in LPS-stimulated WT and *Irg1*^{−/−} mouse macrophages ($n = 3$; LPS 24 h). **d,** Nitrite levels in LPS-stimulated WT and *Irg1*^{−/−} mouse macrophages ($n = 3$; LPS 24 h). **e,** Schematic of metabolic changes occurring during mid-phase TCA cycle rewiring in WT and *Irg1*^{−/−} mouse macrophages ($n = 3$; LPS 4 h). Data are mean ± s.e.m. *P* values calculated using two-tailed Student's t-test for paired comparisons or one-way ANOVA for multiple comparisons.
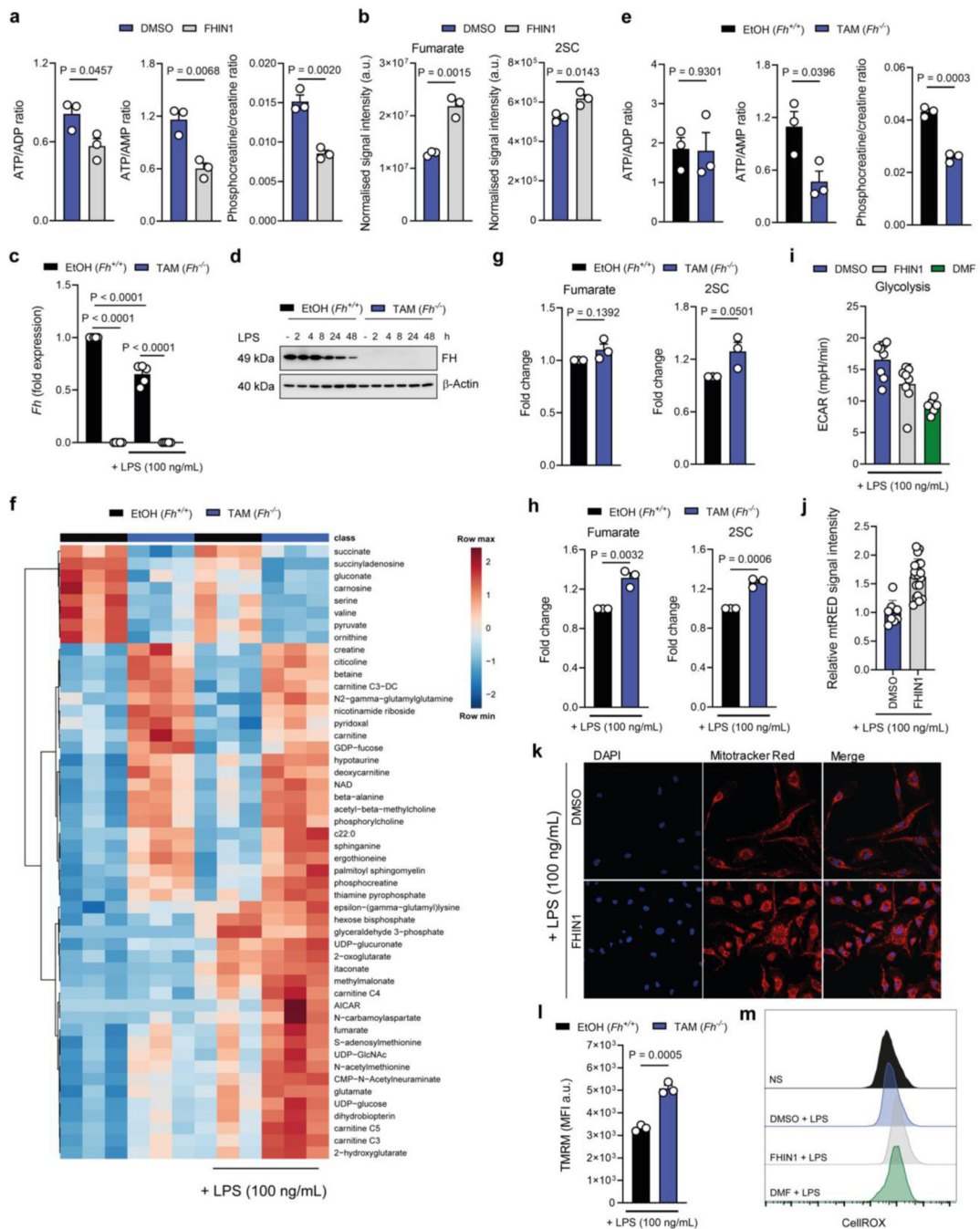
Extended Data Figure 5 –. FH deletion increases bioenergetic stress, fumarate, and mitochondrial membrane potential

a, Bioenergetic ratios in macrophages treated with DMSO or FHIN1 ($n = 3$; LPS 4 h). **b,** Fumarate and 2SC levels in macrophages treated with DMSO or FHIN1 ($n = 3$; LPS 4 h). qPCR ($n = 5$) (**c**) and western blot ($n = 2$) (**d**) analysis of *Fh* expression in *Fh1*$^{+/+}$ and *Fh*$^{-/-}$ LPS-stimulated macrophages (LPS 4 h). **e,** Bioenergetic ratios in *Fh1*$^{+/+}$ and *Fh*$^{-/-}$ macrophages ($n = 3$; LPS 4 h). **f,** Heatmap of top 50 significantly abundant metabolites in LPS-stimulated *Fh1*$^{+/+}$ and *Fh*$^{-/-}$ macrophages ($n = 3$; LPS 4 h). **g, h,** Fumarate and

2SC levels in *Fh1*$^{+/+}$ and *Fh*$^{-/-}$ macrophages treated with or without LPS (n = 3; LPS 4 h). **i,** Glycolysis as measured by ECAR in LPS-stimulated macrophages pre-treated (3 h) with DMSO, FHIN1 or DMF (n = 3; LPS 4 h). Representative experiment shown. Data are mean ± s.d. Immunofluorescence (**k**) and quantification (**j**) of Mitotracker red staining in LPS-stimulated mouse macrophages pre-treated (3 h) with DMSO or FHIN1 (n = 3, LPS 4 h). Representative experiment shown. Data are mean ± s.d. **l,** MFI of TMRM staining in LPS-stimulated *Fh1*$^{+/+}$ and *Fh*$^{-/-}$ macrophages (n = 3; LPS 4 h). **m,** Flow cytometry plot for CellROX staining. **a-c,e,g,h,l** Data are mean ± s.e.m. **d,k,** Representative blots or images shown. P values calculated using two-tailed Student's t-test for paired comparisons or one-way ANOVA for multiple comparisons.
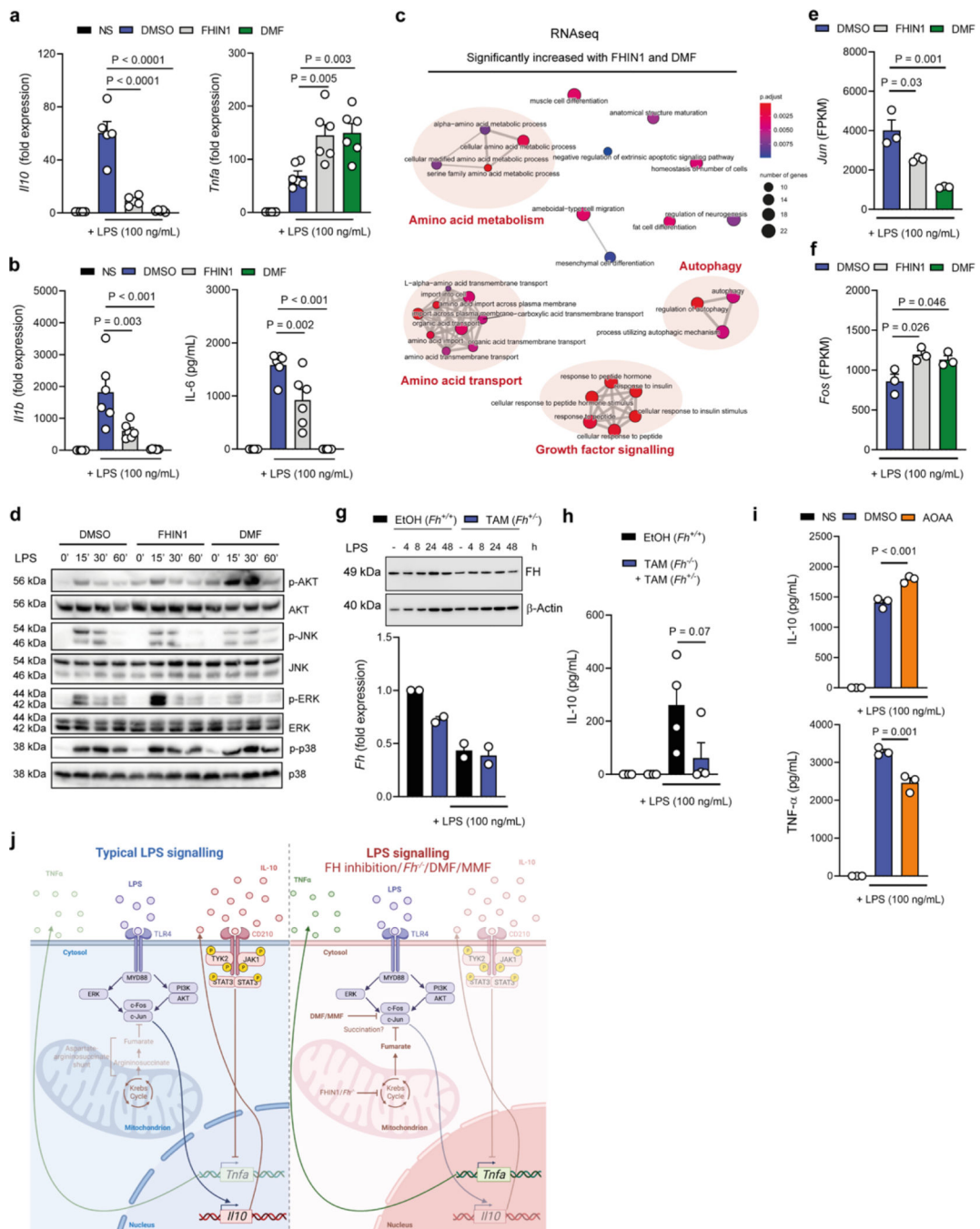
Extended Data Figure 6 –. FH inhibition remodels inflammatory gene expression

a, *Il10* and *Tnfa* expression in LPS-stimulated mouse macrophages pre-treated (3 h) with DMSO, FHIN1 or DMF (n = 4–6; LPS 4 h). **b**, *Il1b* expression and IL-6 release in LPS-stimulated mouse macrophages pre-treated (3 h) with DMSO, FHIN1 or DMF (n = 6; 4 h LPS). **c**, Enrichment map plot of shared significantly increased genes in LPS-stimulated mouse macrophages pre-treated (3 h) with DMF or FHIN1 compared to DMSO control (n = 3; LPS 4 h). **d,** Western blot of total and phospho-AKT, JNK, ERK and p38 levels in LPS-stimulated mouse macrophages pre-treated with DMSO, FHIN1 or DMF (n = 2–3).

e, *Jun* expression from RNA seq from LPS-stimulated mouse macrophages pre-treated (3 h) with DMF or FHIN1 compared to DMSO control ($n = 3$; LPS 4 h). **f,** *Fos* expression from RNA seq from LPS-stimulated mouse macrophages pre-treated (3 h) with DMF or FHIN1 compared to DMSO control (n = 3; LPS 4 h). **g,** FH protein and gene expression levels in *Fh1*$^{+/+}$ and *Fh1*$^{+/-}$ LPS-stimulated macrophages ($n = 2$). **h,** ELISA of IL-10 in LPS-stimulated *Fh*$^{+/+}$ and *Fh1*$^{+/-}$ ($n = 2$)/*Fh*$^{-/-}$ ($n = 2$) macrophages (LPS 4 h). **i,** ELISA of IL-10 and TNF-α release in LPS-stimulated macrophages pre-treated with DMSO or AOAA ($n = 3$; LPS 4 h). **j,** Schematic depicting mild suppression of IL-10 expression during typical LPS signalling (right), and increased suppression of IL-10 following FH inhibition, leading to dysregulated TNF-α release (right). **a,b,e,f,h,i** Data are mean ± s.e.m. **d,g,** Representative blots shown. P values calculated using two-tailed Student's t-test for paired comparisons or one-way ANOVA for multiple comparisons.
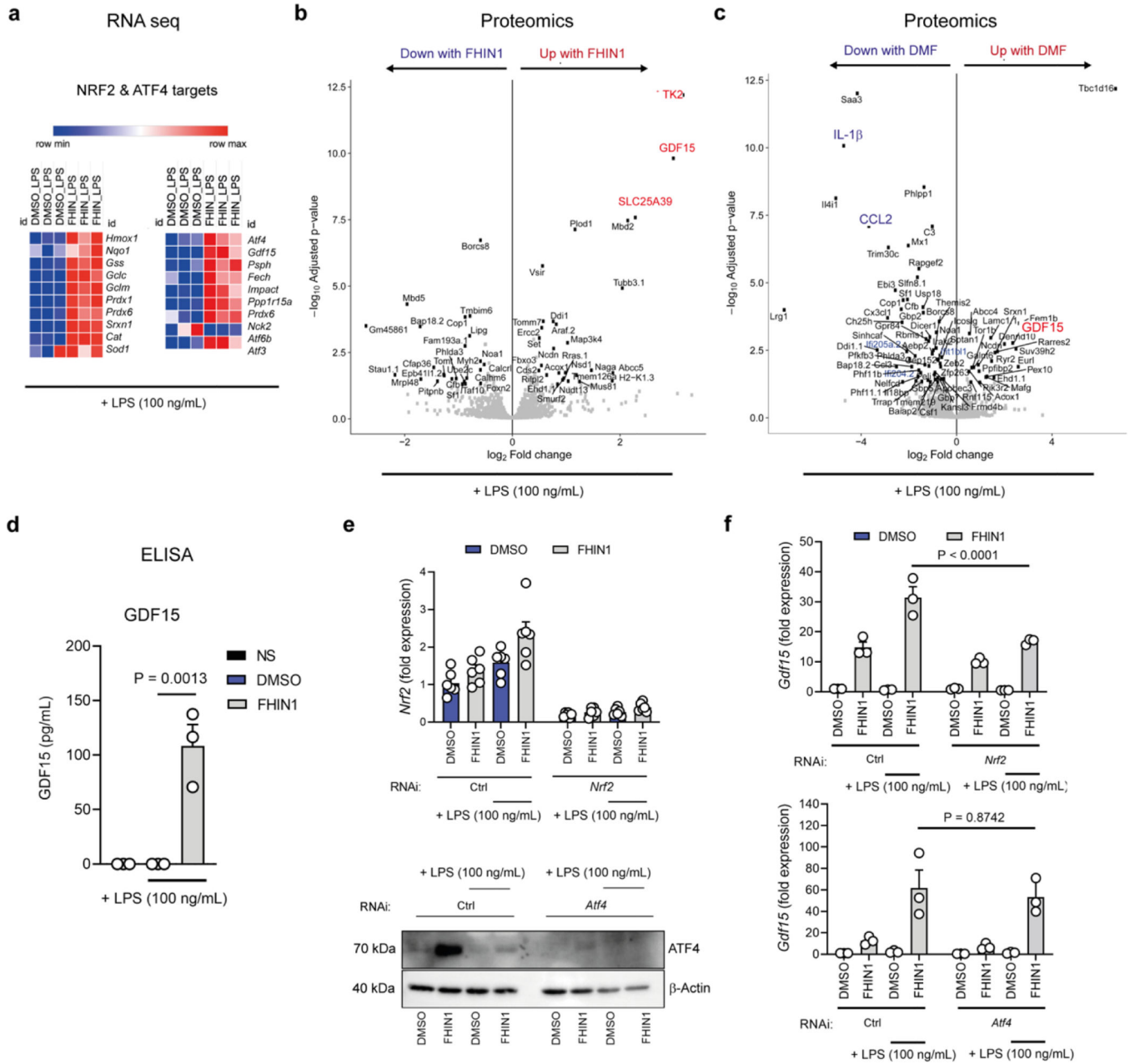
Extended Data Figure 7 –. FH inhibition triggers the NRF2 and ATF4 stress response and promotes GDF15 release

a, Heatmap of significantly differentially expressed mRNA seq data in LPS-stimulated mouse macrophages pre-treated (3 h) with FHIN1 compared to DMSO control (n = 3; LPS 4 h). Volcano plots of proteomics in LPS-stimulated mouse macrophages pre-treated (3 h) with DMSO, FHIN1 (**b**) or DMF (**c**) (n = 5; LPS 4 h). **d,** ELISA of GDF15 in LPS-stimulated macrophages pre-treated (3 h) with DMSO or FHIN1 (*n* = 3; LPS 4 h). **e,** *Nrf2* expression or ATF4 protein levels after silencing of *Nrf2* or *Atf4*, respectively, in NS and LPS-stimulated macrophages pre-treated (3 h) with DMSO or FHIN1 (n = 6; LPS 4 h). **f,** *Gdf15* expression after silencing of *Nrf2* or *Atf4* respectively in NS and LPS-stimulated

macrophages pre-treated (3 h) with DMSO or FHIN1 (*n* = 3, LPS 4 h). **d-f,** Data are mean ± s.e.m. **e,** Representative blots shown. P values calculated using one-way ANOVA for multiple comparisons.
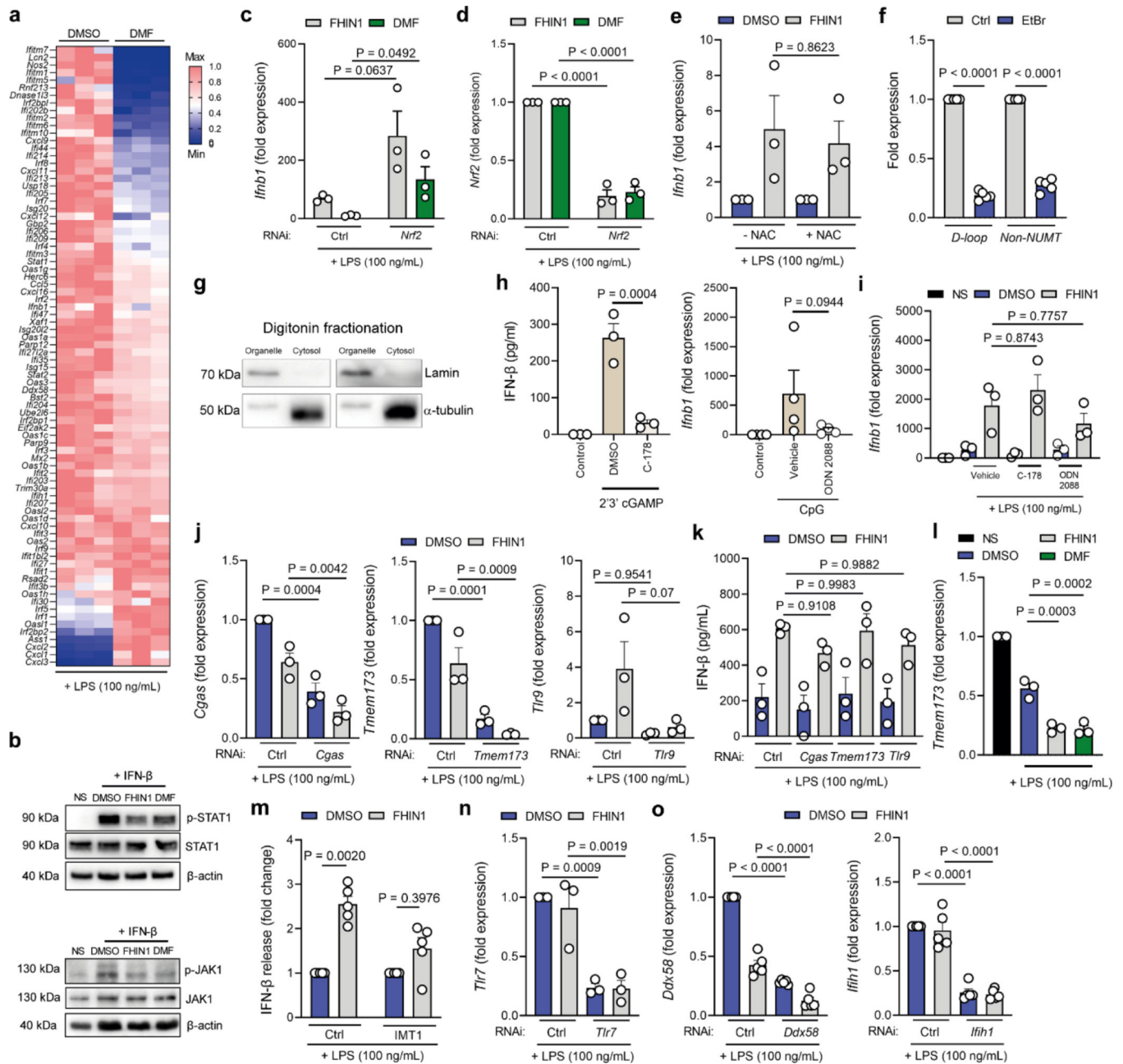
Extended Data Figure 8 –. IFN-β release following FH inhibition is independent of cGAS-STING
a, Heatmap (min-max) of significantly differentially expressed mRNA seq data in LPS-stimulated mouse macrophages pre-treated (3 h) with DMF compared to DMSO control (n = 3; LPS 4 h). **b**, Western blot of phospho-STAT1, STAT1, phospho-JAK1 and JAK1 levels in LPS-stimulated macrophages pre-treated (3 h) with DMSO, FHIN1 or DMF (*n* = 3; LPS 4 h). **c**, *Ifnb1* expression after silencing of *Nrf2* in LPS-stimulated macrophages pre-treated (3

h) with DMSO, FHIN1 or DMF (n = 3, LPS 4 h). **d,** *Nrf2* expression after silencing of *Nrf2* in LPS-stimulated macrophages pre-treated (3 h) with DMSO, FHIN1 or DMF (n = 3, LPS 4 h). **e,** *Ifnb1* expression in LPS-stimulated macrophages pre-treated (3 h) with DMSO or FHIN1 in the presence of absence of NAC (n = 3; LPS 4 h). **f,** *D-loop* and *Non-NUMT* fold expression in EtBr-treated macrophages (n = 5). **g,** Western blot of lamin B1 and α-tubulin in cytosolic and membrane-bound organelle fractions following digitonin fractionation (n = 3). **h**, IFN-β levels in 2',3' cGAMP- or CpG-transfected macrophages pre-treated (1 h) with C-178 or ODN2088 (n = 3–4; 3 h). **i,** *Ifnb1* expression in LPS-stimulated macrophages pre-treated (3 h) with DMSO or FHIN1 in conjunction with C-178 or ODN2088 (1 h) respectively (n = 3; LPS 4 h). **j,** *Cgas, Tmem173* and *Tlr9* expression with silencing of *Cgas, Tmem173* and *Tlr9* respectively in LPS-stimulated macrophages pre-treated (3 h) with DMSO or FHIN1 (n = 3; LPS 4 h). **k,** IFN-β levels with silencing of *Cgas, Tmem173* and *Tlr9* respectively in LPS-stimulated macrophages pre-treated (3 h) with DMSO or FHIN1 (n = 3; LPS 4 h). **l,** *Tmem173* expression in LPS-stimulated macrophages pre-treated (3 h) with DMSO, FHIN1 or DMF (n = 3, LPS 4 h). **m,** IFN-β release (fold change over DMSO control) in LPS-stimulated macrophages pre-treated (3 h) with DMSO or FHIN1 in the presence of absence of IMT1 (n = 5; LPS 4 h). **n,** *Tlr7* expression with silencing of *Tlr7* in LPS-stimulated macrophages pre-treated (3 h) with DMSO or FHIN1 (n = 3; LPS 4 h). **o,** *Ddx58* and *Ifih1* expression with silencing of *Ddx58* and *Ifih1* respectively in LPS-stimulated macrophages pre-treated (3 h) with DMSO or FHIN1 (n = 3; LPS 4 h). **c-f,h-o,** Data are mean ± s.e.m. **b,g,** Representative blots or images shown. P values calculated using two-tailed Student's t-test for paired comparisons or one-way ANOVA for multiple comparisons.
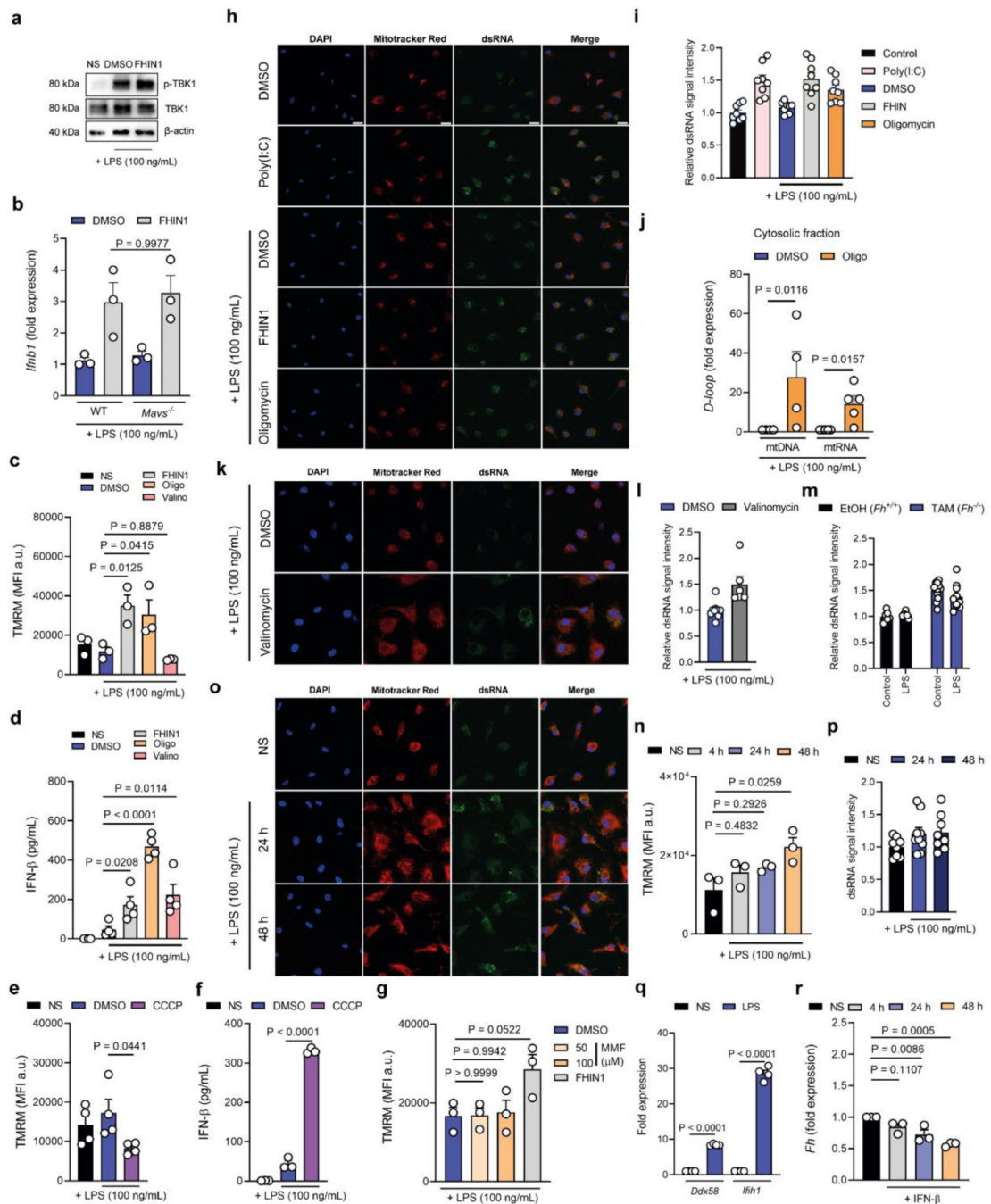
Extended Data Figure 9 –. Mitochondrial membrane potential modifiers increase mtRNA and trigger IFN-β release

a, Western blot of TBK1 and p-TBK1 in LPS-stimulated macrophages pre-treated (3 h) with DMSO or FHIN1 ($n = 3$; LPS 4 h). **b,** *Ifnb1* expression in LPS-stimulated WT and *Mavs*$^{-/-}$ macrophages pre-treated (3 h) with DMSO or FHIN1 ($n = 3$; LPS 4 h). **c,** MFI of TMRM staining in LPS-stimulated macrophages pre-treated (3 h) with DMSO, FHIN1, oligomycin or valinomycin ($n = 3$, LPS 4 h). **d**, IFN-β levels in LPS-stimulated macrophages pre-treated (3 h) with DMSO, FHIN1, oligomycin or valinomycin ($n = 4$;

LPS 4 h).). **e,** MFI of TMRM staining in LPS-stimulated macrophages pre-treated (3 h) with DMSO or CCCP (n = 4, LPS 4 h). **f,** IFN-β levels in LPS-stimulated macrophages pre-treated (3 h) with DMSO or CCCP ($n = 3$; LPS 4 h). **g,** MFI of TMRM staining in LPS-stimulated macrophages pre-treated (3 h) with DMSO or MMF (n = 3, LPS 4 h). Immunofluorescence (**h**) and quantification (**i**) of dsRNA in LPS-stimulated macrophages pre-treated (3 h) with DMSO, FHIN1 or oligomycin or transfected with poly (I:C) ($n = 3$; LPS 4 h). Representative experiment shown. Data are mean ± s.d. **j,** *D-loop* fold expression in DNA and RNA isolated from cytosolic fractions of digitonin-fractionated LPS-stimulated mouse macrophages pre-treated with DMSO or oligomycin ($n = 4$ for mtDNA, $n = 5$ for mtRNA). Immunofluorescence (**k**) and quantification (**l**) of dsRNA in LPS-stimulated macrophages pre-treated with DMSO or valinomycin ($n = 3$; LPS 4 h). Representative experiment shown. Data are mean ± s.d. **m,** Quantification of dsRNA immunofluorescence in LPS-stimulated $Fh^{+/+}$ and $Fh^{-/-}$ macrophages ($n = 3$; LPS 4 h). Data are mean ± s.d. **n,** MFI of TMRM staining in LPS-stimulated macrophages ($n = 3$). Immunofluorescence (**o**) and quantification (**p**) of dsRNA immunofluorescence in LPS-stimulated macrophages ($n = 3$). Representative experiment shown. Data are mean ± s.d. **q,** *Ddx58* and *Ifih1* expression in LPS-stimulated macrophages ($n = 4$; LPS 4 h). **r,** *Fh* expression in IFN-β-stimulated macrophages ($n = 3$). **b-g,j,n,q,r** Data are mean ± s.e.m. **a,h,k,o,** Representative blots or images shown. P values calculated using two-tailed Student's t-test for paired comparisons, one-way ANOVA for multiple comparisons.
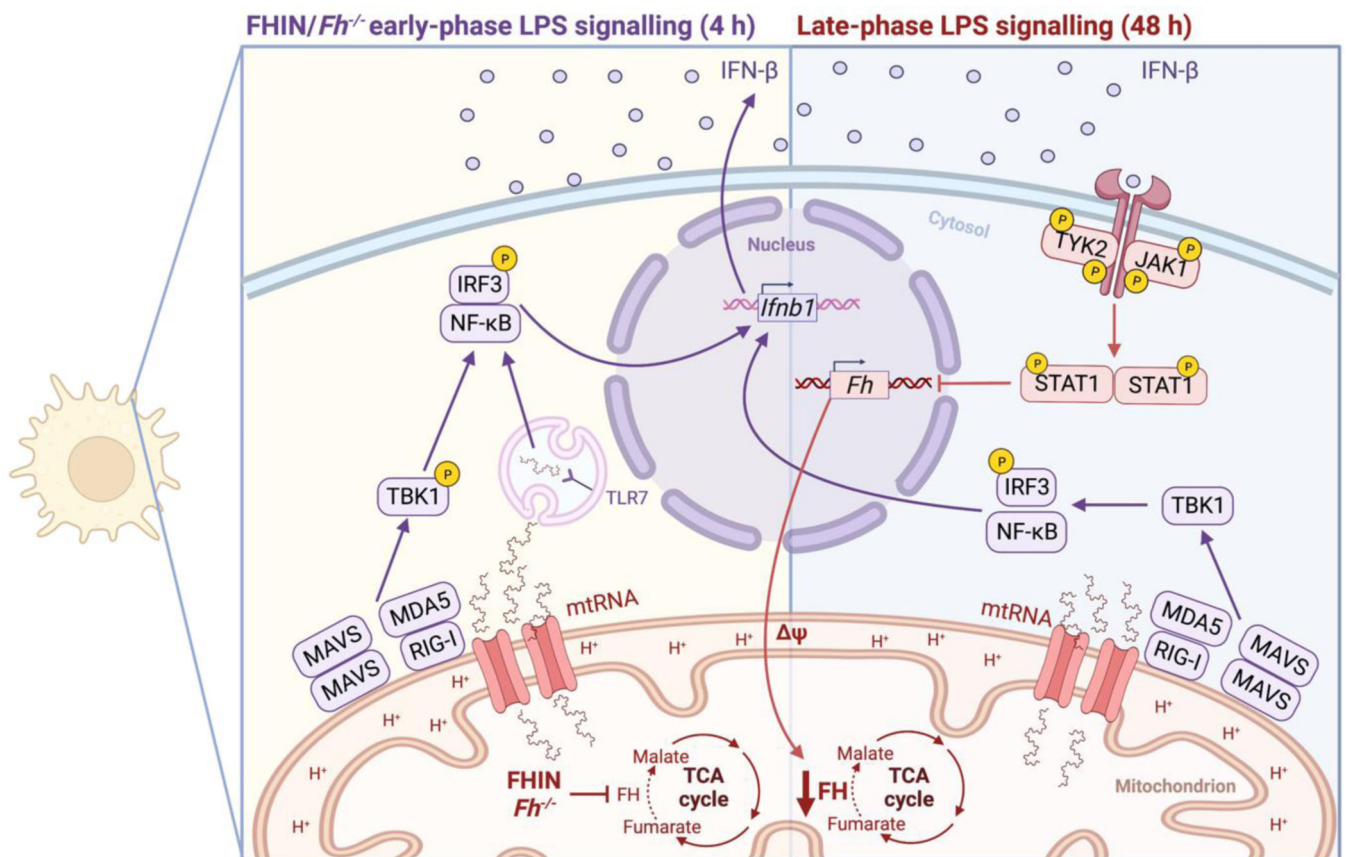
Extended Data Figure 10 –. FH inhibition triggers IFN-β release via a mtRNA-driven retrograde response

Schematic depicting the mitochondrial retrograde signalling cascades occurring following FH inhibition during early-phase LPS signalling (left), and during late-phase LPS signalling in the absence of pharmacological or genetic targeting of FH (right).

Supplementary Material

Refer to Web version on PubMed Central for supplementary material.

Acknowledgements

References

1. Mills EL et al. Succinate dehydrogenase supports metabolic repurposing of mitochondria to drive inflammatory macrophages. Cell 167, 457–470.e13 (2016). [PubMed: 27667687]

2. Mills EL et al. Itaconate is an anti-inflammatory metabolite that activates Nrf2 via alkylation of KEAP1. Nature 556, 113–117 (2018). [PubMed: 29590092]

3. Tannahill GM. et al. . Succinate is an inflammatory signal that induces IL-1β through HIF-1α. Nature 496, 238–242 (2013). [PubMed: 23535595]

4. Lampropoulou V. et al. Itaconate links inhibition of succinate dehydrogenase with macrophage metabolic remodeling and regulation of inflammation. Cell Metab. 24, 158–166 (2016). [PubMed: 27374498]

5. Jha AK et al. Network integration of parallel metabolic and transcriptional data reveals metabolic modules that regulate macrophage polarization. Immunity 42, 419–430 (2015). [PubMed: 25786174]

6. Billingham LK et al. Mitochondrial electron transport chain is necessary for NLRP3 inflammasome activation. Nat. Immunol 23, 692–704 (2022). [PubMed: 35484407]

7. Mills EL, Kelly B. & O'Neill LAJ Mitochondria are the powerhouses of immunity. Nat. Immunol 18, 488–498 (2017). [PubMed: 28418387]

8. Adam J. et al. Renal cyst formation in Fh1-deficient mice is independent of the Hif/Phd pathway: roles for fumarate in KEAP1 succination and Nrf2 signaling. Cancer Cell 20, 524–537 (2011). [PubMed: 22014577]

9. Kornberg MD et al. Dimethyl fumarate targets GAPDH and aerobic glycolysis to modulate immunity. Science 360, 449–453 (2018). [PubMed: 29599194]

10. Humphries F. et al. Succination inactivates gasdermin D and blocks pyroptosis. Science 369, 1633–1637 (2020). [PubMed: 32820063]

11. Williams NC et al. Signaling metabolite L-2-hydroxyglutarate activates the transcription factor HIF-1α in lipopolysaccharide-activated macrophages. J. Biol. Chem 298, 101501 (2021).

12. Cordes T. et al. Immunoresponsive gene 1 and itaconate inhibit succinate dehydrogenase to modulate intracellular succinate levels. J. Biol. Chem 291, 14274–14284 (2016). [PubMed: 27189937]

13. Sass E, Blachinsky E, Karniely S. & Pines O. Mitochondrial and cytosolic isoforms of yeast fumarase are derivatives of a single translation product and have identical amino termini. J. Biol. Chem 276, 46111–46117 (2001). [PubMed: 11585823]

14. Adam J. et al. A role for cytosolic fumarate hydratase in urea cycle metabolism and renal neoplasia. Cell Rep. 3, 1440–1448 (2013). [PubMed: 23643539]

15. Takeuchi T, Schumacker PT & Kozmin SA Identification of fumarate hydratase inhibitors with nutrient-dependent cytotoxicity. J. Am. Chem. Soc 137, 564–567 (2015). [PubMed: 25469852]

16. Ryan DG et al. Disruption of the TCA cycle reveals an ATF4-dependent integration of redox and amino acid metabolism. eLife 10, e72593 (2021).

17. Hayashi G. et al. Dimethyl fumarate mediates Nrf2-dependent mitochondrial biogenesis in mice and humans. Hum. Mol. Genet 26, 2864–2873 (2017). [PubMed: 28460056]

18. Sciacovelli M. et al. Fumarate is an epigenetic modifier that elicits epithelial-to- mesenchymal transition. Nature 537, 544–547 (2016). [PubMed: 27580029]

19. Wang YP et al. Malic enzyme 2 connects the Krebs cycle intermediate fumarate to mitochondrial biogenesis. Cell Metab. 33, 1027–1041 e1028 (2021). [PubMed: 33770508]

20. Liao ST et al. 4-Octyl itaconate inhibits aerobic glycolysis by targeting GAPDH to exert anti-inflammatory effects. Nat. Commun 10, 5091 (2019). [PubMed: 31704924]

21. Crooks DR et al. Mitochondrial DNA alterations underlie an irreversible shift to aerobic glycolysis in fumarate hydratase-deficient renal cancer. Sci. Signal 14, eabc4436 (2021).

22. Blatnik M, Frizzell N, Thorpe SR & Baynes JW Inactivation of glyceraldehyde3-phosphate dehydrogenase by fumarate in diabetes: formation of S-(2-succinyl) cysteine, a novel chemical modification of protein and possible biomarker of mitochondrial stress. Diabetes 57, 41–49 (2008). [PubMed: 17934141]

23. Tyrakis PA et al. Fumarate hydratase loss causes combined respiratory chain defects. Cell Rep. 21, 1036–1047 (2017). [PubMed: 29069586]

24. Ternette N. et al. Inhibition of mitochondrial aconitase by succination in fumarate hydratase deficiency. Cell Rep. 3, 689–700 (2013). [PubMed: 23499446]

25. Sullivan LB et al. The proto-oncometabolite fumarate binds glutathione to amplify ROS-dependent signaling. Mol. Cell 51, 236–248 (2013). [PubMed: 23747014]

26. Zheng L. et al. Fumarate induces redox-dependent senescence by modifying glutathione metabolism. Nat. Commun 6, 6001 (2015). [PubMed: 25613188]

27. Bambouskova M. et al. Electrophilic properties of itaconate and derivatives regulate the IκBζ–ATF3 inflammatory axis. Nature 556, 501–504 (2018). [PubMed: 29670287]

28. Raimundo N, Vanharanta S, Aaltonen LA, Hovatta I. & Suomalainen A. Downregulation of SRF–FOS–JUNB pathway in fumarate hydratase deficiency and in uterine leiomyomas. Oncogene 28, 1261–1273 (2009). [PubMed: 19151755]

29. Hu X. et al. IFN-γ suppresses IL-10 production and synergizes with TLR2 by regulating GSK3 and CREB/AP-1 proteins. Immunity 24, 563–574 (2006). [PubMed: 16713974]

30. Angel P, Hattori K, Smeal T. & Karin M. The *jun* proto-oncogene is positively autoregulated by its product, Jun/AP-1. Cell 55, 875–885 (1988). [PubMed: 3142689]

31. Dickinson SE et al. Inhibition of activator protein-1 by sulforaphane involves interaction with cysteine in the cFos DNA-binding domain: implications for chemoprevention of UVB-induced skin cancer. Cancer Res. 69, 7103–7110 (2009). [PubMed: 19671797]

32. de Waal Malefyt R, Abrams J, Bennett B, Figdor CG & de Vries JE Interleukin 10 (IL-10) inhibits cytokine synthesis by human monocytes: an autoregulatory role of IL-10 produced by monocytes. J. Exp. Med 174, 1209–1220 (1991). [PubMed: 1940799]

33. Luan HH et al. GDF15 is an inflammation-induced central mediator of tissue tolerance. Cell 178, 1231–1244.e11 (2019). [PubMed: 31402172]

34. Day EA et al. Metformin-induced increases in GDF15 are important for suppressing appetite and promoting weight loss. Nat. Metab 1, 1202–1208 (2019). [PubMed: 32694673]

35. Coll AP et al. GDF15 mediates the effects of metformin on body weight and energy balance. Nature 578, 444–448 (2020). [PubMed: 31875646]

36. Wang Y. et al. SLC25A39 is necessary for mitochondrial glutathione import in mammalian cells. Nature 599, 136–140 (2021). [PubMed: 34707288]

37. Weng JH et al. Colchicine acts selectively in the liver to induce hepatokines that inhibit myeloid cell activation. Nat. Metab 3, 513–522 (2021). [PubMed: 33846641]

38. Eisenstein A. et al. Activation of the transcription factor NRF2 mediates the anti-inflammatory properties of a subset of over-the-counter and prescription NSAIDs. Immunity 55, 1082–1095.e5 (2022). [PubMed: 35588739]

39. Asadullah K. et al. Influence of monomethylfumarate on monocytic cytokine formation—explanation for adverse and therapeutic effects in psoriasis? Arch. Dermatol. Res 289, 623–630 (1997). [PubMed: 9444385]

40. Arts RJ et al. Glutaminolysis and fumarate accumulation integrate immunometabolic and epigenetic programs in trained immunity. Cell Metab. 24, 807–819 (2016). [PubMed: 27866838]

41. Ryan DG et al. Nrf2 activation reprograms macrophage intermediary metabolism and suppresses the type I interferon response. iScience 25, 103827 (2022).

42. Shanmugasundaram K. et al. The oncometabolite fumarate promotes pseudohypoxia through noncanonical activation of NF-κB signaling. J. Biol. Chem 289, 24691–24699 (2014). [PubMed: 25028521]

43. West AP et al. Mitochondrial DNA stress primes the antiviral innate immune response. Nature 520, 553–557 (2015). [PubMed: 25642965]

44. Sliter DA et al. Parkin and PINK1 mitigate STING-induced inflammation. Nature 561, 258–262 (2018). [PubMed: 30135585]

45. McArthur K. et al. BAK/BAX macropores facilitate mitochondrial herniation and mtDNA efflux during apoptosis. Science 359, eaao6047 (2018).

46. Dang EV, McDonald JG, Russell DW & Cyster JG Oxysterol restraint of cholesterol synthesis prevents AIM2 inflammasome activation. Cell 171, 1057–1071.e11 (2017). [PubMed: 29033131]

47. Haag SM et al. Targeting STING with covalent small-molecule inhibitors. Nature 559, 269–273 (2018). [PubMed: 29973723]

48. Stunz LL et al. Inhibitory oligonucleotides specifically block effects of stimulatory CpG oligonucleotides in B cells. Eur. J. Immunol 32, 1212–1222 (2002). [PubMed: 11981808]

49. Prantner D. et al. 5,6-Dimethylxanthenone-4-acetic acid (DMXAA) activates stimulator of interferon gene (STING)-dependent innate immune pathways and is regulated by mitochondrial membrane potential. J. Biol. Chem 287, 39776–39788 (2012). [PubMed: 23027866]

50. Dhir A. et al. Mitochondrial double-stranded RNA triggers antiviral signalling in humans. Nature 560, 238–242 (2018). [PubMed: 30046113]

51. Tigano M, Vargas DC, Tremblay-Belzile S, Fu Y. & Sfeir A. Nuclear sensing of breaks in mitochondrial DNA enhances immune surveillance. Nature 591, 477–481 (2021). [PubMed: 33627873]

52. Kariko K, Buckstein M, Ni H. & Weissman D. Suppression of RNA recognition by Toll-like receptors: the impact of nucleoside modification and the evolutionary origin of RNA. Immunity 23, 165–175 (2005). [PubMed: 16111635]

53. Rai P. et al. IRGM1 links mitochondrial quality control to autoimmunity. Nat. Immunol 22, 312–321 (2021). [PubMed: 33510463]

54. Kruger A. et al. Human TLR8 senses UR/URR motifs in bacterial and mitochondrial RNA. EMBO Rep. 16, 1656–1663 (2015). [PubMed: 26545385]

55. Pichlmair A. et al. . RIG-I-mediated antiviral responses to single-stranded RNA bearing 5′-phosphates. Science 314, 997–1001 (2006). [PubMed: 17038589]

56. Koshiba T, Yasukawa K, Yanagi Y. & Kawabata S. Mitochondrial membrane potential is required for MAVS-mediated antiviral signaling. Sci. Signal 4, ra7 (2011). [PubMed: 21285412]

57. Kim S. et al. Mitochondrial double-stranded RNAs govern the stress response in chondrocytes to promote osteoarthritis development. Cell Rep. 40, 111178 (2022).

58. Rasa SMM et al. Inflammaging is driven by upregulation of innate immune receptors and systemic interferon signaling and is ameliorated by dietary restriction. Cell Rep. 39, 111017 (2022).

59. Buskiewicz IA et al. Reactive oxygen species induce virus-independent MAVS oligomerization in systemic lupus erythematosus. Sci. Signal 9, ra115 (2016).

60. Ruiz-Limon P. et al. Atherosclerosis and cardiovascular disease in systemic lupus erythematosus: effects of in vivo statin treatment. Ann. Rheum. Dis 74, 1450–1458 (2015). [PubMed: 24658835]

61. Davis P, Cunnington P. & Hughes GR Double-stranded RNA antibodies in systemic lupus erythematosus. Ann. Rheum. Dis 34, 239–243 (1975). [PubMed: 1155982]

62. Caielli S. et al. Oxidized mitochondrial nucleoids released by neutrophils drive type I interferon production in human lupus. J. Exp. Med 213, 697–713 (2016). [PubMed: 27091841]

63. Sarkar P. et al. Reduced expression of mitochondrial fumarate hydratase in progressive multiple sclerosis contributes to impaired in vitro mesenchymal stromal cell-mediated neuroprotection. Mult. Scler 28, 1179–1188 (2022). [PubMed: 34841955]

64. Zecchini V. et al. Fumarate induces vesicular release of mtDNA to drive innate immunity. Nature 10.1038/s41586-023-05770-w (2023).

65. Li Q. et al. RNA editing underlies genetic risk of common inflammatory diseases. Nature 608, 569–577 (2022). [PubMed: 35922514]

66. Pang Z. et al. MetaboAnalyst 5.0: narrowing the gap between raw spectra and functional insights. Nucleic Acids Res. 49, W388–W396 (2021). [PubMed: 34019663]

67. Anders S. & Huber W. Differential expression analysis for sequence count data. Genome Biol. 11, R106 (2010). [PubMed: 20979621]

68. Shah AD, Goode RJA, Huang C, Powell DR & Schittenhelm RB LFQ-Analyst: an easy-to-use interactive web platform to analyze and visualize label-free proteomics data preprocessed with MaxQuant. J. Proteome Res 19, 204–211 (2020). [PubMed: 31657565]

69. Kuleshov MV et al. Enrichr: a comprehensive gene set enrichment analysis web server 2016 update. Nucleic Acids Res. 44, W90–W97 (2016). [PubMed: 27141961]

70. Subramanian A. et al. Gene set enrichment analysis: a knowledge-based approach for interpreting genome-wide expression profiles. Proc. Natl Acad. Sci. USA 102, 15545–15550 (2005). [PubMed: 16199517]
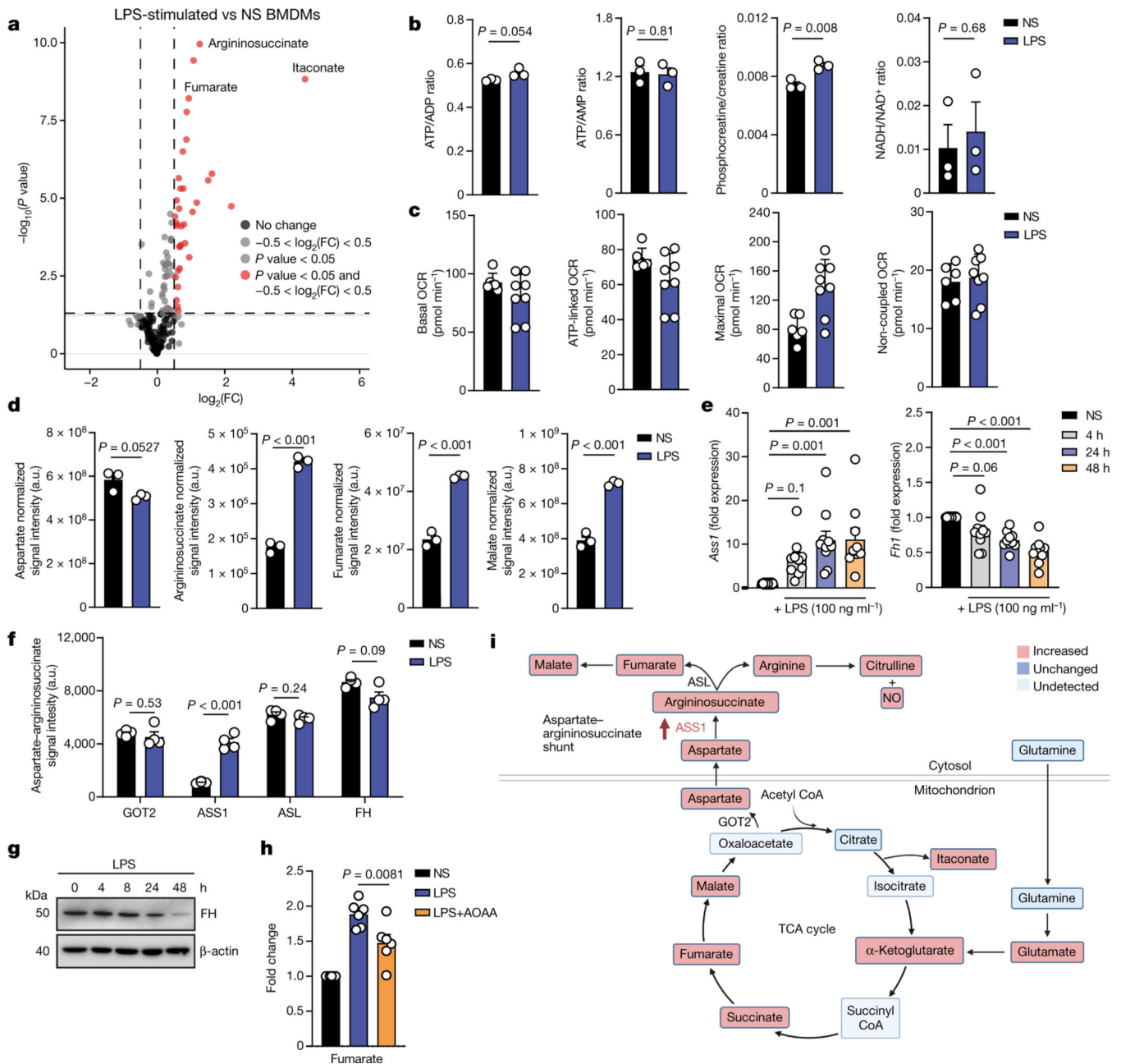
Fig. 1 |. LPS stimulation drives fumarate accumulation through glutamine anaplerosis and an aspartate–argininosuccinate shunt.

a,b,d, Metabolite abundance (**a,d**) and bioenergetic ratios (**b**) in non-stimulated (NS) and LPS-stimulated BMDMs ($n = 3$). LPS 4 h: argininosuccinate, $P = 0.000044$; fumarate, $P = 0.000141$; malate, $P = 0.000219$. a.u., arbitrary units; FC, fold change. **c**, Respirometry as measured by oxygen consumption rates (OCRs) of NS and LPS-stimulated BMDMs ($n = 6$ (NS) or 8 (LPS); LPS 4 h). $n =$ technical replicates from 1 experiment performed with 3 pooled biological replicates. Data are mean ± s.d. **e**, *Ass1* and *Fh1* gene expression with LPS time course ($n = 9$). LPS 24 h, $P = 0.000729$; LPS 48 h, $P = 0.000001$. **f**, Quantitative proteomics of aspartate–argininosuccinate shunt enzymes in NS and LPS-

stimulated BMDMs ($n = 4$). LPS 24 h: ASS1, $P = 0.000156$. **g**, FH levels with LPS time course ($n = 1$). **h**, Fumarate levels following LPS stimulation with or without AOAA pre-treatment (1 h) ($n = 6$, LPS 4 h). **i**, Schematic of metabolic changes occurring during early-phase TCA cycle rewiring (LPS 4 h). For **b,d–f,h**, data are mean ± s.e.m. $n =$ biological replicates unless stated otherwise. P values calculated using two-tailed Student's t-test for paired comparisons or one-way analysis of variance (ANOVA) for multiple comparisons. Schematic in panel **i** was created using BioRender (https://biorender.com).
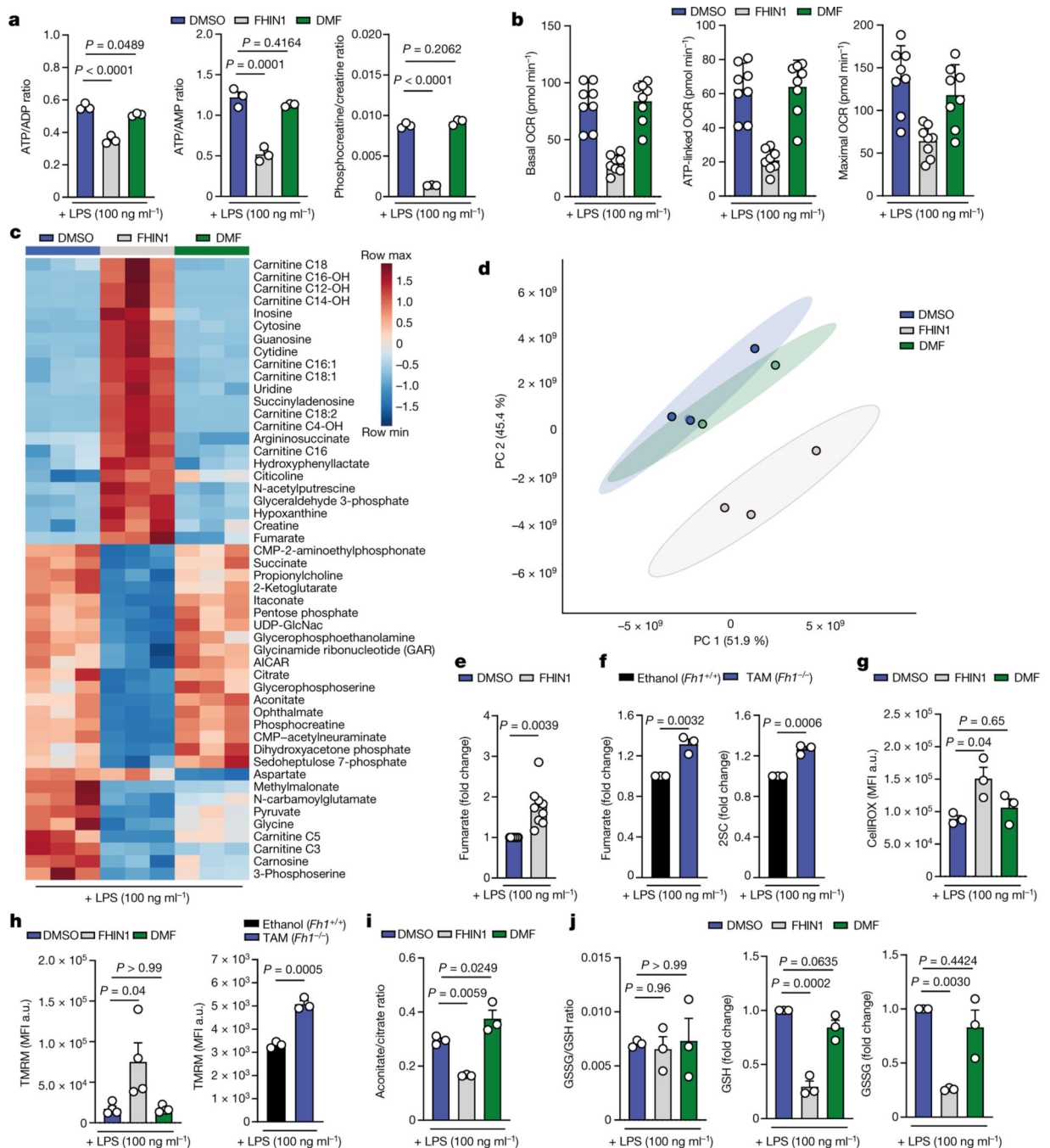
Fig. 2 |. FH inhibition increases bioenergetic stress, fumarate levels and MMP.
a,c, Bioenergetic ratios (**a**) and heatmap of top 50 differentially abundant metabolites (**c**) in BMDMs pre-treated with vehicle (DMSO), FHIN1 or DMF (n = 3). LPS 4 h: ATP/ADP, P = 0.000004; phosphocreatine/creatine, P = 0.00000001. **b**, Respirometry of BMDMs pre-treated with DMSO, FHIN1 or DMF (n = 8; LPS 4 h). n = technical replicates from 1 experiment performed with 3 pooled biological replicates. Data are mean ± s.d. **d**, Principal component analysis plot of metabolomics in BMDMs pre-treated with DMSO, FHIN1 or DMF (n = 3; LPS 4 h). **e**, Fumarate levels in BMDMs pre-treated with DMSO or FHIN1

(n = 9; LPS 4 h). **f**, Fumarate and 2SC levels in $Fh1^{+/+}$ and $Fh1^{-/-}$ BMDMs (n = 3; 96 h ethanol and 4-hydroxytamoxifen (TAM); LPS 4 h). **g**, Mean fluorescence intensity (MFI) of CellROX staining in BMDMs pre-treated with DMSO, FHIN1 or DMF (n = 3; LPS 4 h). **h**, MFI of TMRM staining in BMDMs pre-treated with DMSO, FHIN1 or DMF or $Fh1^{+/+}$ and $Fh1^{-/-}$ BMDMs (n = 4 (DMSO, FHIN1 and DMF) or n = 3 ($Fh1^{+/+}$ and $Fh1^{-/-}$); 72 h ethanol and TAM; LPS 4 h). **i**, Aconitate/citrate ratio following LPS stimulation with or without FHIN1 or DMF pre-treatment (n = 3; LPS 4 h). **j**, GSH and GSSG levels following LPS stimulation with or without FHIN1 or DMF pre-treatment (n = 3; LPS 4 h). For **a**,**e**–**j**, data are mean ± s.e.m. n = biological replicates unless stated otherwise. P values calculated using two-tailed Student's t-test for paired comparisons or one-way or ANOVA for multiple comparisons.
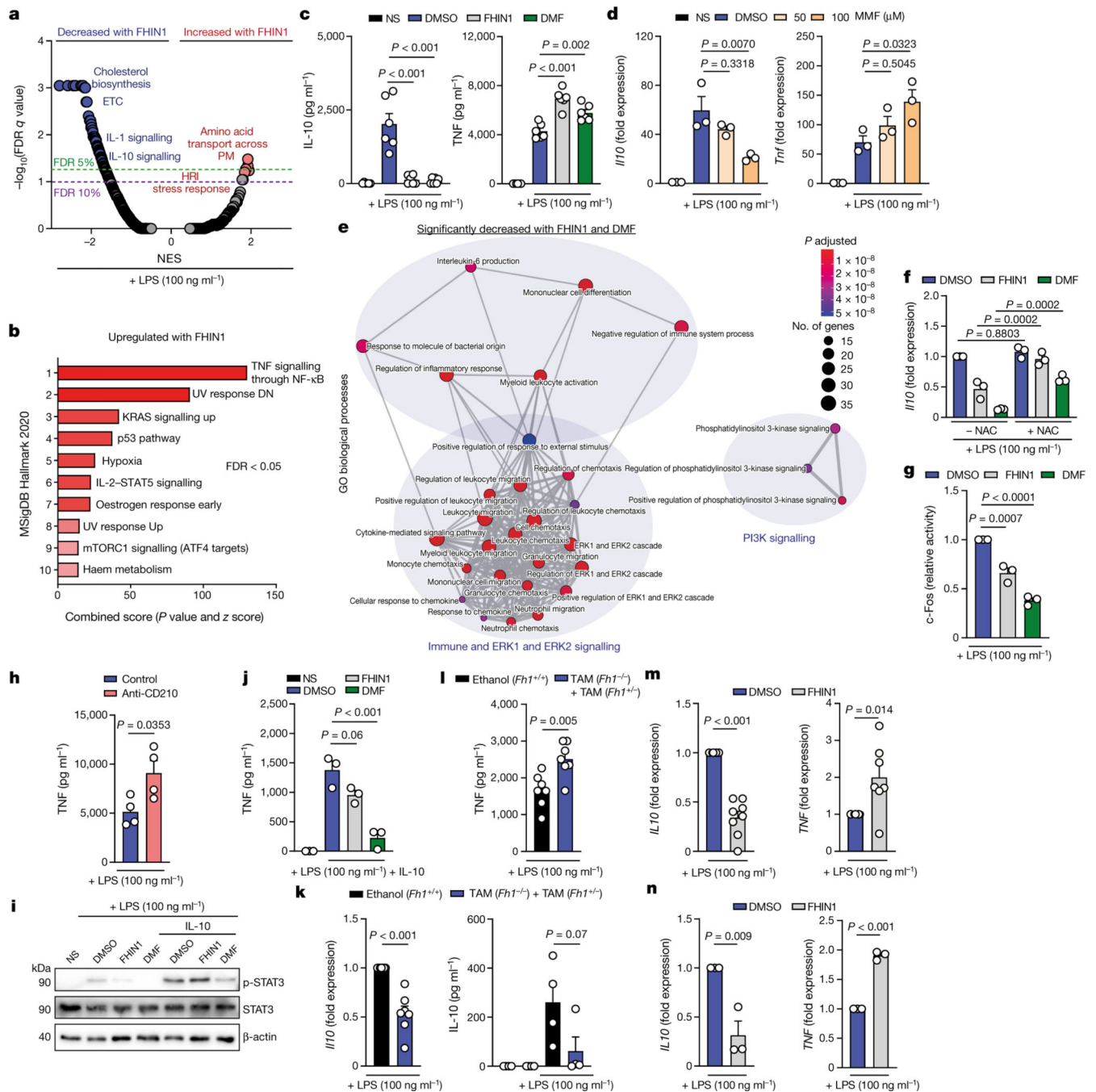
Fig. 3 |. FH activity is required to maintain appropriate cytokine responses.
a,b, GSEA (**a**) and overrepresentation analysis (**b**) of RNA-seq data of BMDMs pre-treated with FHIN1 or DMSO ($n = 3$; LPS 4 h). HRI, haem-regulated inhibitor. **c**, IL-10 and TNF release from BMDMs pre-treated with DMSO, FHIN1 or DMF ($n = 6$; LPS 4 h). FHIN1 and IL-10, $P = 0.0000024$; DMF and IL-10, $P = 0.0000018$; FHIN1 and TNF, $P = 0.000001$. **d**, *Il10* and *Tnf* expression in BMDMs pre-treated with DMSO or MMF ($n = 3$; LPS 4 h). **e**, Enrichment map plot of shared significantly decreased genes in BMDMs pre-treated with FHIN1 or DMF ($n = 3$; LPS 4 h). **f**, *Il10* expression in BMDMs pre-treated with

DMSO, FHIN1 or DMF in the presence of NAC ($n = 3$; LPS 4 h). **g**, c-Fos activity in BMDMs pre-treated with DMSO, FHIN1 or DMF ($n = 3$; LPS 4 h). DMF, $P = 0.0000298$. **h**, TNF release from BMDMs pre-treated with anti-CD210 antibody (1 h) ($n = 4$; LPS 4 h). **i,j**, Western blot for STAT3 and phospho-STAT3 (pSTAT-3; **i**) and TNF release (**j**) from BMDMs pre-treated with DMSO, FHIN1 or DMF and treated with IL-10 ($n = 3$, LPS 4 h).DMF, $P = 0.000163$. **k**, *Il10* expression and IL-10 release in *Fh1*$^{+/+}$ and *Fh1*$^{-/-}$ ($n = 5$ or 2) and *Fh1*$^{+/-}$ ($n = 2$) BMDMs (ethanol and TAM 72 h; LPS 4 h). *Il10*,$P = 0.000055$. **l**, TNF release from *Fh1*$^{+/+}$ and *Fh1*$^{-/-}$ ($n = 5$) and *Fh1*$^{+/-}$ ($n = 2$) BMDMs (ethanol and TAM 72 h; LPS 4 h). **m**, *IL10* and *TNF* expression in human PBMCs pre-treated with DMSO or FHIN1 ($n = 8$, LPS 4 h). FHIN1, $P = 0.00000008$. **n**, *IL10* and *TNF* expression in human macrophages pre-treated with DMSO or FHIN1 ($n = 3$, LPS 4 h) FHIN1, $P = 0.000028$. For **c**,**d**,**f**–**h**,**j**–**n**, data are mean ± s.e.m. For **i**, blot is representative of three. n = biological replicates. P values calculated using two-tailed Student's t-test for paired comparisons or one-way ANOVA for multiple comparisons.
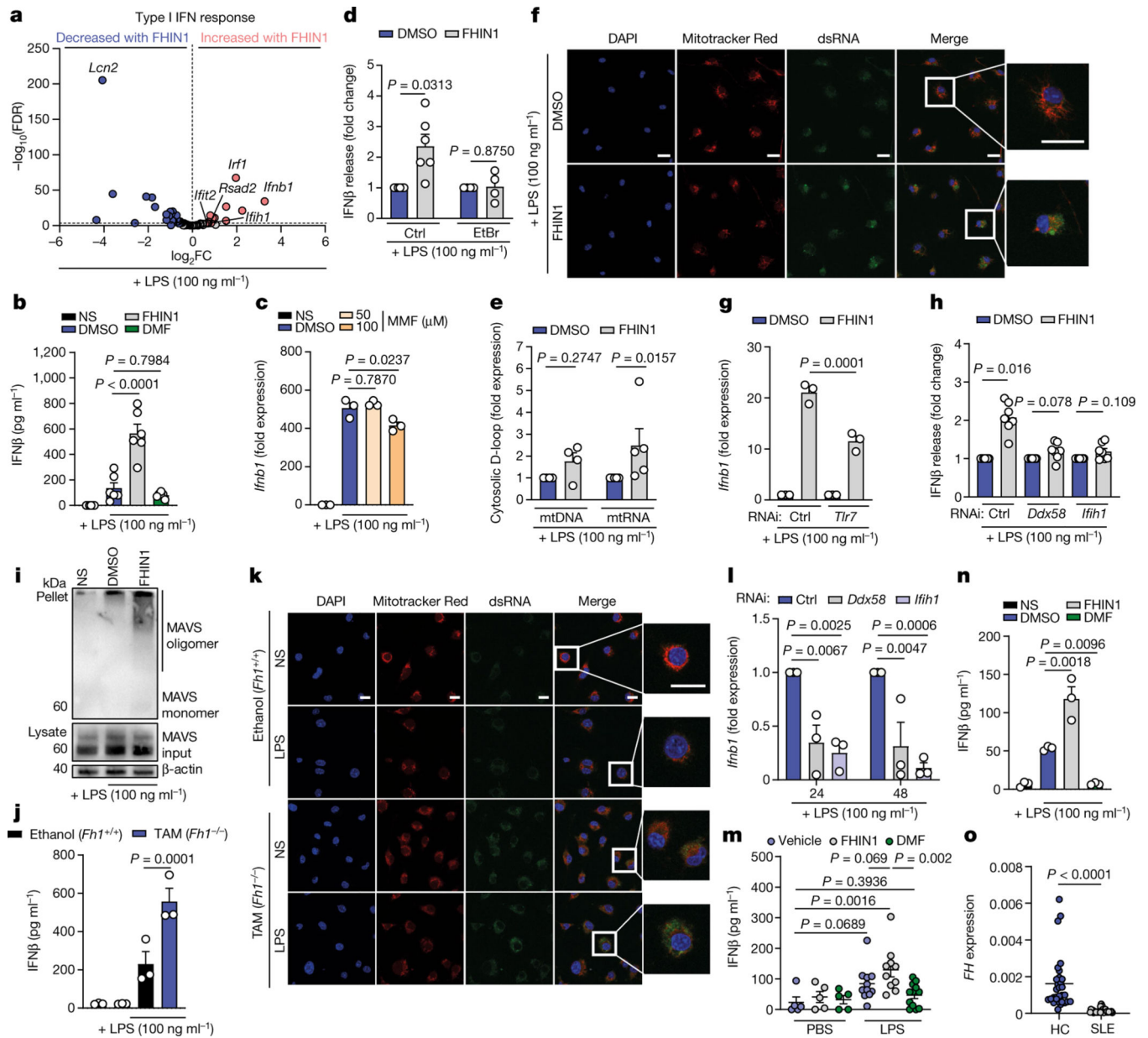
Fig. 4 |. FH impairment triggers IFNβ release through a mtRNA-driven retrograde response.
a, Volcano plot of type I IFN response in BMDMs pre- treated with DMSO or FHIN1 (*n* = 3; LPS 4 h). **b**, IFNβ release from BMDMs pre- treated with DMSO, FHIN1 or DMF (*n* = 6; LPS 4 h). FHIN1, *P* = 0.000004. **c**, *Ifnb1* expression in BMDMs pre-treated with DMSO or MMF (*n* = 3; LPS 4 h). **d**, IFNβ release from BMDMs treated with ethidium bromide (EtBr) (for 6 days) before pre-treatment with DMSO or FHIN1 (*n* = 6; LPS 4 h). Ctrl, control. **e**, Cytosolic D-loop expression in DNA and RNA in BMDMs pre-treated with DMSO or FHIN1 (*n* = 4 (mtDNA) or 5 (mtRNA); LPS 4 h). **f**, dsRNA immunofluorescence in BMDMs pre-treated with DMSO or FHIN1 (*n* = 3; LPS 4 h). **g**, *Ifnb1* with *Tlr7* silencing in BMDMs pre-treated with DMSO or FHIN1 (*n* = 3; LPS 4 h). **h**, IFNβ with *Ddx58* or *Ifih1* silencing in BMDMs pre-treated with DMSO or FHIN1 (*n* = 7; LPS 4 h). **i**, MAVS in

BMDMs pre-treated with DMSO or FHIN1 ($n = 3$; LPS 4 h). **j**, IFNβ levels in $Fh1^{+/+}$ and $Fh1^{-/-}$ BMDMs ($n = 3$; ethanol and TAM 72 h; LPS 4 h). **k**, dsRNA immunofluorescence in $Fh1^{+/+}$ and $Fh1^{-/-}$ BMDMs ($n = 3$; ethanol and TAM 72 h; LPS 4 h). **l**, *Ifnb1* with *Ddx58* or *Ifih1* silencing ($n = 3$). **m**, Serum IFNβ of mice treated with FHIN1 or DMF before PBS or LPS injection ($n = 5$ (PBS), 10 (FHIN1 and LPS), 11 (vehicle and LPS) or 12 (DMF and LPS)). **n**, IFNβ release from human PBMCs pre-treated with DMSO, FHIN1 or DMF ($n = 3$; LPS 4 h). **o**, *FH* expression in whole blood from healthy individuals (HC) and patients with SLE ($n = 30$; $P = 0.0000005$). For **b–e,g,h,j,l–o**, data are mean ± s.e.m. For **f,i,k**, blot or image is representative of three experiments. n = biological replicates. P values calculated using two-tailed Student's *t*-test for paired comparisons, one-way ANOVA for multiple comparisons. Scale bars, 20 μm (**f,k**).